available at www.sciencedirect.com

ScienceDirect

journal homepage: www.sciencedirect.com/journal/chinese-journal-of-catalysis

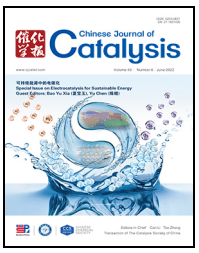

Review

Electrocatalytic generation of reactive species and implications in microbial inactivation

Forrest Nichols [a], Kenneth I. Ozoemena [b], Shaowei Chen [a,*]

[a] *Department of Chemistry and Biochemistry, University of California, 1156 High Street, Santa Cruz, California 95064, United States*
[b] *Molecular Sciences Institute, School of Chemistry, University of the Witwatersrand, Private Bag 3, P.O. Wits, Johannesburg 2050, South Africa*

ARTICLE INFO

Article history:
Received 15 July 2021
Accepted 8 September 2021
Available online 20 April 2022

Keywords:
Electrocatalysis
Reactive species
Microorganism
Inactivation
Water electrodisinfection

ABSTRACT

Controlling microbial proliferation in water systems, including wastewater, recreational water, and drinking water, is essential to societal health. Microbial inactivation through electrochemically generated reactive species (RS) mediated pathways provides an effective route toward this microbial control. Herein we provide an overview of recent progress toward electrocatalytic generation of RS and their application in water disinfection, with a focus on the selective production of RS, the microorganism interactions with RS (including both RS mechanisms of action and innate microorganism responses to RS), and practical implementation of electrochemically generated RS for microbial inactivation. The article is concluded with a perspective where the challenges and opportunities of RS-based electrochemical disinfection of water are highlighted, along with possible future research directions.

1. Introduction

Assurance of safe and healthy water is critical for progress of life on earth. Many methods for water disinfection have been implemented, including physical, biological, and chemical pathways [1]. A chemical route toward water disinfection typically involves the use of advanced processes to remove contaminants through oxidation. Several advanced oxidative processes (AOP) have already been implemented into water treatment, including ozonation and UV light [2]. The field of electrochemistry provides another viable pathway toward efficient water disinfection, which also poses a sustainable pathway as electricity supply becomes increasingly renewable [3]. Water treatment by AOP primarily focusses on production of highly oxidizing substances, such as hydroxyl radicals (HO•); however, significant research has been dedicated in recent literature to the electrochemical generation of many other reactive species (RS), including reactive oxygen species (ROS) like superoxide ($O_2^{\bullet-}$) and hydrogen peroxide (H_2O_2), reactive chlorine species (RCS), reactive nitrogen species (RNS), as well as reactive sulfur species (RSS), which can also be used in the water treatment process [4–7].

Numerous microorganisms have been found to transmit diseases through water systems, including bacteria, viruses, protozoa, and helminths [8]. It is essential for humans to treat these threats during the water disinfection process. Bacteria are particularly susceptible to the presence of RS with damage to proteins, DNA, and lipid membranes leading to cell death [4–7]. This makes electrochemical generation of RS an attractive pathway toward microbial inactivation during water treatment (Fig. 1).

There are several distinct advantages of electrochemical RS generation over other methods such as photocatalysis. One major advantage is the ability for an electrochemical device to

* Corresponding author. E-mail: shaowei@ucsc.edu
This work was supported by the National Science Foundation (CBET-1848841, CHE-1900235).
DOI: 10.1016/S1872-2067(21)63941-4 | http://www.sciencedirect.com/journal/chinese-journal-of-catalysis | Chin. J. Catal., Vol. 43, No. 6, June 2022

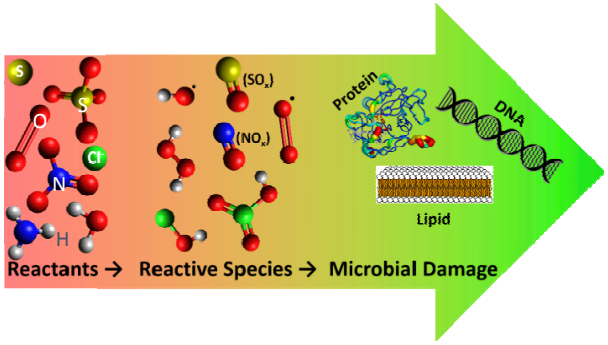

Fig. 1. Schematic representation of the electrosynthesis of RS and corresponding targets for microbial damage. Spheres represent oxygen (red), hydrogen (grey), chlorine (green), sulfur (yellow), and nitrogen (blue) atoms.

disinfect a wide variety of contaminated water including particularly cloudy or murky water that would otherwise prevent the transmittance of light through the water medium necessary for photocatalytic treatment. Another distinct advantage is the ability to have fine control over the input energy source, electricity, during the decontamination process. Other advantages and disadvantages of electrochemical RS generation will be discussed below throughout the review.

We begin this review outlining the primary RS studied in recent electrocatalysis research, with a focus on the electrochemical conditions and RS reactivity, and provide a context into recent reports of the deliberate design and engineering of relevant electrocatalysts. We then outline how these RS interact with microbial organisms leading to microbial inactivation. We conclude the review by summarizing recent work involving the generation of specific RS toward microbial inactivation with a prospective of the field and what is needed to progress the current technologies.

2. Electrocatalytic generation of reactive species

2.1. Reactive oxygen species

Organisms that rely on aerobic respiration as a means of energy production are required to interact with molecular oxygen, as it is the final electron acceptor in the electron transport chain. At the end of aerobic respiration, the fourth and final enzyme in the electron transport chain, cytochrome C oxidase, catalyzes the reduction of molecular oxygen to water [9–19]. Like the oxygen reduction reaction (ORR) in fuel cell electrocatalysis, the conversion of molecular oxygen to water in a biological cell is not without error and can lead to toxic oxygen byproducts, such as superoxide ($O_2^{\bullet-}$) and hydrogen peroxide (H_2O_2) [16–24]. Production of these species during electrocatalysis is often categorized as an undesirable effect; however, production of such ROS can be advantageous under controlled conditions. From an electrochemistry perspective, researchers are beginning to design electrocatalysts capable of efficiently producing ROS for many applications, including industrial hydrogen peroxide production, organic molecule synthesis, microbial inactivation, water disinfection, electrocoagulation, and other contaminant disinfection (*e.g.*, organic dye degradation) [4–7,25–32].

Electrochemical ROS generation can occur on the cathode by reduction of molecules, including molecular oxygen, or at the anode through oxidation of adsorbates, such as water. A proposed stepwise mechanism for generating such ROS is depicted in Reaction (1), flowing from left to right for the reduction processes and right to left for the oxidation processes [33].

$$O_2 \leftrightarrows O_2^{\bullet-} \leftrightarrows H_2O_2 \leftrightarrows HO^{\bullet} \leftrightarrows H_2O \quad (1)$$

From Reaction (1), we can see that there are three primary ROS products, superoxide, hydrogen peroxide, and hydroxyl radical. In the following sections, we will explore in further detail the relationship between these species, their chemical reactivity, and relevant electrocatalysts reported recently for the synthesis of these species.

2.1.1. Superoxide ($O_2^{\bullet-}$)

Generation of $O_2^{\bullet-}$ in electrochemical systems can occur by a one-electron reduction of adsorbed oxygen at the cathode surface, as shown by Reaction (2), with a formal potential (E^0) of +0.330 V *vs.* reversible hydrogen electrode (RHE). $O_2^{\bullet-}$ can also be produced by the oxidation of H_2O_2 following Reaction (3). $O_2^{\bullet-}$ generation has been studied primarily in aprotic solvents, such as dimethyl sulfoxide (DMSO), as $O_2^{\bullet-}$ quickly reacts in protic solvents forming O_2 and hydroperoxide anion (HO_2^-), the conjugate base of H_2O_2, as shown in Reaction (4), with a short half-life of only 5 s at physiological pH, which renders it difficult to harvest for actual bacterial control applications [34–36].

$$O_2 + e^- \rightarrow O_2^{\bullet-} \quad (2)$$

$$H_2O_2 \rightarrow O_2^{\bullet-} + 2H^+ + e^- \quad (3)$$

$$O_2^{\bullet-} + H_2O \rightarrow O_2 + HO_2^- + HO^{\bullet} \quad (4)$$

2.1.2. Hydrogen peroxide (H_2O_2)

Relative to $O_2^{\bullet-}$, H_2O_2 has a long half-life of ca. 1 h in protic solvents and at physiological pH with spontaneous disproportionation occurring by Reaction (5) [37]. Thus, H_2O_2 can be collected and used for an array of applications. Electrochemical generation of H_2O_2 has been extensively studied alongside fuel cell research [33,38–43], where H_2O_2 is produced through a two-electron process either by the reduction of O_2 (E^0 = 1.230 V *vs.* RHE) or oxidation of H_2O (E^0 = 1.760 V *vs.* RHE), shown by Reactions (6) and (7), respectively.

$$H_2O_2 \rightarrow H_2O + \tfrac{1}{2}O_2 \quad (5)$$

$$O_2 + 2H^+ + 2e^- \rightarrow H_2O_2 \quad (6)$$

$$2H_2O \rightarrow H_2O_2 + 2H^+ + 2e^- \quad (7)$$

$$O_2 + 4H^+ + 4e^- \rightarrow 2H_2O \quad (8)$$

In fact, hydrogen peroxide generation at the cathode during ORR has been rather extensively studied as a side reaction occurring in fuel cell electrocatalysis [44–49]. Classical fuel cell research aims to design electrocatalysts which facilitate the complete reduction of oxygen to water *via* the four-electron pathway shown in Reaction (8) and avoid possible peroxide generation, to maximize the electrocatalytic performance and minimize corrosion of the fuel cell device.

However, for water disinfection purposes, generation of hydrogen peroxide can be advantageous, as manifested in a series

of earlier studies [50–52]. H_2O_2 is sometimes used as a precursor to produce homogeneous HO• *via* the electro-Fenton process. Heterogeneous HO• can also be produced directly at the electrode surface and will be discussed further in the next section of this review. It should be noted that homogeneous and heterogeneous HO• may be produced in tandem for improved decontamination efficiency. For instance, Brillas and co-workers [53] successfully demonstrated this application in their study of the degradation of monoazo, diazo, and triazo dyes using an electrochemical setup consisting of a carbon-ploytetrafluoroethylene (PTFE) air-diffusion cathode and a boron doped diamond anode (BDD). Carbon-PTFE has been used widely as a cathode for the two-electron reduction of oxygen forming H_2O_2 [54–56], while BDD has been extensively studied as an inactive anode for the direct production of heterogeneous HO• [57–61]. It was found that dye degradation occurred to both heterogeneous HO• created at the BDD anode and homogeneous HO• produced by the electro-Fenton process, where H_2O_2, produced at the carbon-PTFE cathode, reacted with added Fe^{2+}.

Recently, researchers have also studied electrocatalysts specifically designed to allow ORR *via* the two-electron pathway shown in Reaction (6), and single atom catalysts (SACs) have emerged as a unique and powerful platform that can selectively catalyze the two-electron reduction of oxygen to hydrogen peroxide [62], due to the possibility of tailoring the catalytic activity through deliberate modifications to the single atom coordination environment [62]. For instance, Tang and co-workers [63] recently reported on a Mo SAC with unique O and S coordination towards two-electron ORR. The material was synthesized through a two-step process involving hydrothermal synthesis of MgO nanosheets from bulk MgO followed by calcination and a final carbonization step incorporating S from a benzyl disulfide precursor. The SAC structure was confirmed by high-angle annular dark-field scanning transmission electron microscopy (HAADF-STEM), X-ray photoelectron spectroscopy (XPS), extended X-ray absorption fine structure (EXAFS), and Wavelet transform-EXAFS (WT-EXAFS) analysis. Fig. 2(a) depicts a pseudo-color surface plot produced from the HAADF-STEM images for the obtained Mo_1/OSG-H sample, where single Mo atoms (blue) were deposited on a carbon matrix (green) with significant defect sites (yellow). Fig. 2(b) shows the real-space EXAFS spectra for Mo_1/OSG-H, bulk MoS_2, bulk molybdenum oxide (Na_2MoO_4), and bulk molybdenum foil. Mo_1/OSG-H exhibited a primary peak near 1.2 Å, which was assigned to Mo-O coordination, and the lack of spectral features at longer distance suggested virtually no Mo-Mo interactions, in agreement with HAADF-STEM findings. Electrochemical tests with a rotating ring-disk electrode (RRDE) in a three-electrode electrochemical setup were carried out to assess the material's ability to catalyze H_2O_2 formation from molecular oxygen, revealing 95% selectivity under these conditions. First principles density functional theory (DFT) calculations were then employed to better understand the significance of the Mo-O/Mo-S coordination environments (Fig. 2(c)), and the results revealed preferential OOH* adsorption on C adjacent to Mo (Mo-O_4-C), with electron transfer occurring from Mo to adsorbed OOH*, as evidenced in Bader charge calculations (the asterisk denotes a species adsorbed onto the catalyst surface). Notably, the adsorption was significantly improved upon S incorporation

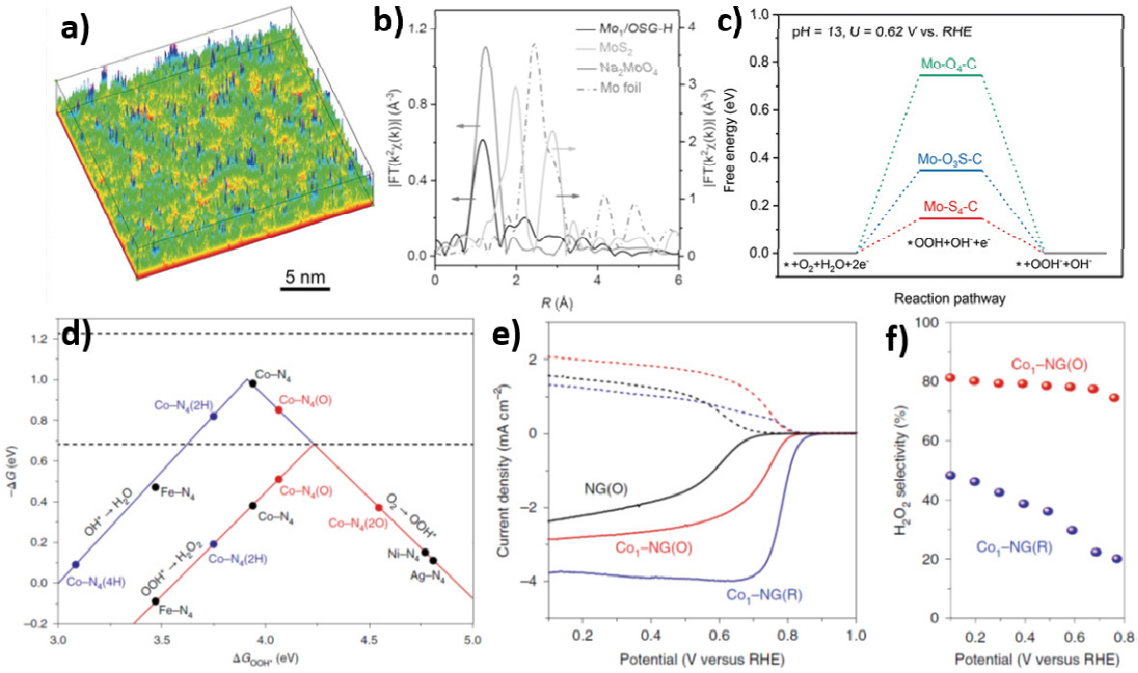

Fig. 2. (a) Pseudo-color surface plot created from HAADF-STEM image of Mo_1/OSG-H. (b) FT-EXAFS curves at Mo *K* edge. (c) Free energy diagram of $2e^-$ ORR on three substrates at equilibrium potential. (a–c) Reproduced with permission from Ref. [63], Copyright 2020, Wiley-VCH. (d) Volcano plots for ORR producing water (blue) and H_2O_2 (red). Solid lines are created from the calculations of various M-N_4 species (M = Co, Ni, Fe, and Ag). (e) Polarization curves for NG(O) (black), Co_1-NG(O) (red), and Co_1-NG(R) (blue) with currents from the disk (solid) and ring (dashed) electrodes. (f) H_2O_2 selectivity measured for Co_1-NG(O) (red) and Co_1-NG(R) (blue) over the potential range of 0.1–0.8 V *vs.* RHE. Measurements performed at 1600 rpm rotation rate in 0.1 mol/L KOH. (d–f) Reproduced with permission from Ref. [64], Copyright 2020, Springer Nature.

(Mo-O_3S-C), and a further increase of S loading resulted in improved OOH* binding strength and reduced free energy of adsorbed OOH* intermediate (Mo-S_4-C).

Jung and co-workers [64] also highlighted the ability to optimize the electrocatalytic performance through engineering SAC coordination environment in their recent report of a CoN_4 catalyst toward two-electron reduction of molecular oxygen to H_2O_2. They began their work by studying the relationship between M-N_4/graphene moieties and ORR selectivity through DFT calculations forming adjacent volcano plots that corresponded to catalyst selectivity toward the two- or four-electron reduction of oxygen (Fig. 2(d)). It was demonstrated through first principles DFT calculations that the OOH* free energy (ΔG_{OOH*}) on the CoN_4/graphene moiety can be tailored by the addition of electron-rich oxygen functional groups around the CoN_4 centers, due to a slight increase of the Co charge state and optimization of ΔG_{OOH*}. These findings were indeed confirmed experimentally. Three samples were prepared by controlled pyrolysis, one containing only graphene oxide (GO) (NG(O)), another with cobalt single atoms embedded in GO (Co_1-NG(O)), and a third one with cobalt single atoms embedded in reduced graphene oxide (Co_1-NG(R)). Co_1-NG(O) was found to contain 6.6 at.% oxygen, while only 2.1 at% for Co_1-NG(R). ORR tests were then carried out with a three-electrode setup and an RRDE as the working electrode, and the results (Fig. 2(e)) from collection experiments revealed a substantial current response at the ring electrode with the Co_1-NG(O) sample (red curve), in comparison to the metal-free NG(O) (black curve) and oxygen-deficient (Co_1-NG(R) (blue curve). The corresponding H_2O_2 selectivity (Fig. 2(f)) was estimated to be 80% for Co_1-NG(O), markedly higher than that (<50%) for Co_1-NG(R). Results from this study provided a unique method for tailoring the electrocatalyst selectivity toward H_2O_2 generation through controlled oxygen functionality within the GO support.

In these previous studies, theoretical calculations were employed to assist the rational design of effective electrocatalysts for two-electron reduction of O_2 to H_2O_2. Another side of the same coin can be found in the work toward H_2O_2 production through the two-electron water oxidation reaction (2e⁻ WOR, Reaction (7)). As mentioned previously, the oxidizing conditions typically require large overpotentials, due to the thermodynamic constraints in the water oxidation processes. Thus, materials selected for this electrocatalytic process are often metal oxides capable of handling large overpotentials applied over an extended period of time. For example, Shi and co-workers [65] prepared various metal oxide electrocatalysts toward H_2O_2 *via* 2e⁻ WOR. DFT calculations were carried out to evaluate the limiting potentials as a function of OH* adsorption energy for the 2e⁻ and 4e⁻ WOR processes, as shown by the black and blue curves in Fig. 3(a), respectively. Important WOR intermediates include OH*, O*, and OOH*. These intermediates arise from the 1e⁻, 2e⁻, and 4e⁻ oxidation of water, respectively. OH* is the first intermediate produced in WOR and its adsorption energy often dictates reaction products, where strong OH* binding typically follows the 4e⁻ WOR, while weak OH* binding leads to 2e⁻ WOR and H_2O_2 generation [66]. Therefore, OH* binding was chosen as the descriptor in identifying possible candidates for 2e⁻ WOR electrocatalysts. Of the four metal oxides, WO_3(100) (black triangle), SnO_2(110) (blue square), TiO_2(110) (pink diamond), and $BiVO_4$(111) (red circle), where the facet was selected based on stability for each material (Fig. 3(a)), the calculated onset potentials were found to be consistent with the experimental results, increasing in the order of WO_3 < $BiVO_4$ < SnO_2 < TiO_2 (Fig. 3(b)). However, $BiWO_4$ was observed to have the greatest selectivity among the series of materials at 70%, resulting in the highest H_2O_2 production rate of ca. 6 mol min^{-1} cm^{-2}.

In a more recent report, Kelly and colleagues [67] demonstrated improved activity and selectivity of a unique ZnO(10$\bar{1}$0) material toward 2e⁻ WOR. To better understand the WOR pathways, a free energy diagram was constructed beginning with water, including intermediate steps, and possible reaction products such as OH•, H_2O_2, and O_2, as shown in Fig. 3(c). To facilitate 2e⁻ WOR on ZnO, the ideal adsorption energy of the OH* intermediate (ΔG_{OH*}) was determined to be in the range of 1.6 to 2.4 eV, shown by the green shaded region in Fig. 3(d),

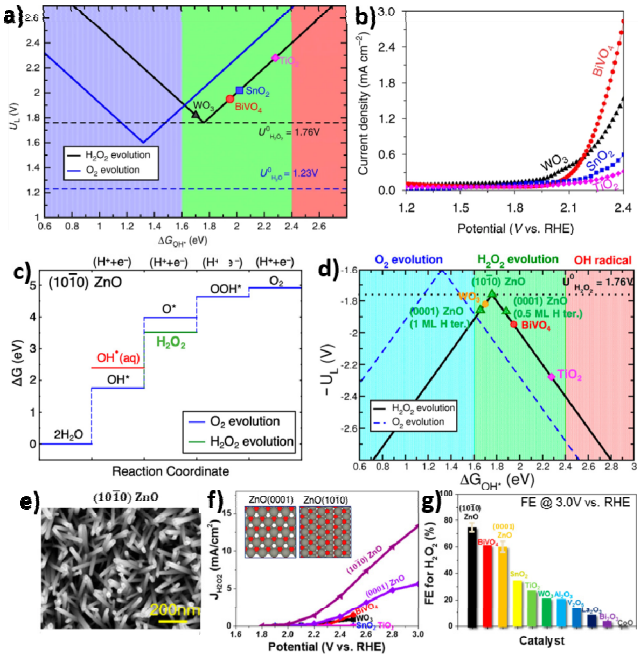

Fig. 3. (a) Volcano plot of electrocatalytic activity corresponding to limiting potential *vs.* OH* adsorption energy for 2e⁻ (black) and 4e⁻ (blue) WOR. Equilibrium potentials are shown in dashed lines. (b) Polarization curves for four select metal oxides toward 2e⁻ WOR. (a,b) Reprinted with permission from Ref. [66]. Copyright 2015, Springer Nature. (c) Free energy diagram for the stepwise O_2 evolution reaction (blue) and H_2O_2 evolution reaction (green) with 4 intermediate steps; (d) Volcano plots produced from calculated limiting potential (U_L) as a function of OH* binding free energy (ΔG_{OH*}) for the four-electron water oxidation (blue dashed line) and two electron water oxidation to H_2O_2 (black line). Three favorable reaction pathways are highlighted by shading O_2 evolution (blue), H_2O_2 evolution (green), and OH• production (red). (e) SEM images of ZnO(10$\bar{1}$0) nanorods. (f) Catalytic activity of 2e⁻ WOR in 2 mol/L potassium bicarbonate of ZnO(10$\bar{1}$0), Zn(0001) and other metal oxides. Inset depicts model representations of the ZnO(0001) and ZnO(10$\bar{1}$0) crystal structures. (g) Faraday Efficiency (FE) at 3.0 V vs RHE for ZnO(10$\bar{1}$0), as compared to various other metal oxide materials with error bars taken from 5 independent measurements. (c–g) Reprinted with permission from Ref. [67], Copyright 2019, American Chemical Society.

such that the binding of OH* is not too strong, leading to 4e⁻ WOR, or too weak, leading to OH* desorption and OH• generation. All ZnO facets studied in this report were determined to have ΔG_{OH^*} within this idealized range. The limiting potentials for these various ZnO facets were then calculated, and the ZnO($10\bar{1}0$) facet was found to possess the lowest limiting potential and thus the highest predicted 2e⁻ WOR rate. Motivated by these theoretical results, ZnO with predominant ($10\bar{1}0$) facets was synthesized on fluorine-doped tin oxide (FTO) glass and characterized by scanning electron microscopy (SEM) (Fig. 3(e)), transmission electron microscopy (TEM), and X-ray diffraction (XRD) measurements. Electrochemical measurements revealed outstanding 2e⁻ WOR selectivity and reaction rate with ZnO($10\bar{1}0$), as compared to that with Zn(0001) and results reported previously in the literature with relevant metal oxides (Fig. 3(f)). In fact, ZnO($10\bar{1}0$) exhibited a faradaic efficiency (FE) over 80% and a current density of 0.1 mA cm^{-2} at a low overpotential of 40 mV, much better than various other oxide materials reported under similar reaction conditions (Fig. 3(g)).

In summary, with a sufficiently long half-life for the inactivation of bacteria, H_2O_2 can be produced through the partial reduction of oxygen or partial oxidation of water, where the design and engineering of relevant electrocatalysts plays a critical role. Towards this end, SACs have emerged as high-performance electrocatalysts for the selective production of H_2O_2. The key advantage of SACs over conventional catalysts lies in the maximal atom efficiency and mass activity, a unique feature to optimize the use of precious metals added and minimize the catalyst cost. Table S1 lists additional electrocatalysts for H_2O_2 generation in recent studies. In the following section we will examine the relationship between H_2O_2 and HO•.

2.1.3. Hydroxyl radical (HO•)

H_2O_2 can undergo homolytic fission to produce two hydroxyl radicals with substantial oxidizing capability, as depicted in Reaction (9), due to the high standard reduction potential (E^0 = 2.330 V *vs*. RHE) of Reaction (10) [68].

$$H_2O_2 \rightarrow 2HO^{\bullet} \quad (9)$$

$$HO^{\bullet} + H^+ + e^- \rightarrow H_2O \quad (10)$$

Note that Reaction (9) is readily facilitated by the addition of ferrous (Fe^{2+}) ions *via* the Fenton reaction, which was first reported in 1894 [69,70]. Utilizing this premise, one may facilitate the formation of HO• through the addition of ferrous ions into the electrolyte medium containing an H_2O_2 electrocatalyst. This is commonly referred to as the electro-Fenton process and has been studied with success in recent literature reports [71–74]. For instance, Li and co-workers [75] employed nitrogen-doped graphene to catalyze the production of H_2O_2 and subsequent HO• upon the addition of ferrous ion *via* the electro-Fenton process. Experimentally, N-doped graphene was synthesized by using a modified Hummer's method followed by a carbonization step with the addition of dopamine hydrochloride as the nitrogen source. The resulting N-doped graphene was combined with graphite felt (GF) through a secondary annealing process to create the N-doped graphene/GF catalyst. RRDE tests were then carried out to examine the electrocatalytic activity for the 2e⁻ reduction of oxygen to H_2O_2, which was confirmed by analysis of the Koutecky-Levich (KL) plots, and further supported by results from hydroxyl radical scavenger probes and electron spin resonance (ESR) measurements with the addition of 0.5 mmol/L Fe^{2+} to the electrolyte solution (0.05 mol/L Na_2SO_4). Notably, the composite catalyst was found to be active in the degradation of phenacetin for wastewater treatment purposes, achieving a 98% degradation rate after 2 h of electrocatalysis at an applied current density of 7 mA cm^{-2}.

In a more recent study, Sheng and co-workers [74] studied the electro-Fenton chemistry of cobalt selenide with samples prepared by hydrothermal selenization of cobalt hydroxide carbonate hydrate followed by thermal annealing, which removed excess selenium and was used to control the $CoSe_2$ polymorphism. Low-temperature annealing was found to produce orthorhombic marcasite-$CoSe_2$ (o-$CoSe_2$), while annealing above 300 °C resulted in complete transition to cubic pyrite-$CoSe_2$ (c-$CoSe_2$). Cubic cobalt sulfide (c-CoS_2) was also produced for comparison. Based on spin polarized electronic structure calculations with the Vienna *ab initio* simulation package (VASP), the obtained surface Pourbaix diagrams revealed OH* surface coverage at the cobalt sites for both o-$CoSe_2$ and c-$CoSe_2$ polymorphs at low overpotentials. Note that 4e⁻ reduction of molecular oxygen requires sufficient O_2 binding and cleaving of the O–O bond, whereas a high Co–OH* surface coverage prevents O_2 binding to Co and subsequent O–O bond cleavage. Thus, the high surface coverage of OH* on the cobalt site was determined to be beneficial for selective 2e⁻ ORR, as shown in Fig. 4(a). In fact, electrochemical measurements showed that the H_2O_2 selectivity decreased in the order of o-$CoSe_2$ > c-$CoSe_2$ > c-CoS_2, due to the increased Co–OH* surface coverage at low to moderate overpotentials on o-$CoSe_2$. Fig. 4(b) shows the corresponding kinetic current density for H_2O_2 generation. One can see that within the potential range of 0.5 to 0.7 V, the current density decreases in the order of c-$CoSe_2$ (green) > o-$CoSe_2$ (red) > c-CoS_2 (blue), and they are all markedly greater than results reported previously for other 2e⁻ ORR catalysts. o-$CoSe_2$ was then used in the degradation of rhodamine B (RhB) dye *via* the electro-Fenton process in a Na_2SO_4 (0.5 mol/L) electrolyte containing 0.5 mmol/L Fe^{2+} at 0.5 V *vs*. RHE. Complete degradation of rhodamine B (RhB, 20 mg L^{-1}) occurred within 20 min. As current generation was not correlated to RhB degradation during the chronoamperometric measurements, RhB removal was most likely due to the produced hydroxyl radicals rather than direct degradation of RhB in contact with the electrode surface.

The electro-Fenton process is a useful technique, but it would be desirable in many applications to remove the requirement for added ferrous ions and catalyze HO• formation directly using an electrocatalyst. Heterogeneous SACs are an ideal candidate for this process, since a series of studies have shown that homolytic fission of H_2O_2 can occur on select SACs. For example, Wu and co-workers recently developed a SAC containing isolated copper atoms through a two-part synthesis process [76]. Experimentally, copper nitrate was mixed into solutions of melamine and cyanuric acid, where a small amount of solution-phase copper was trapped within the strong hy-

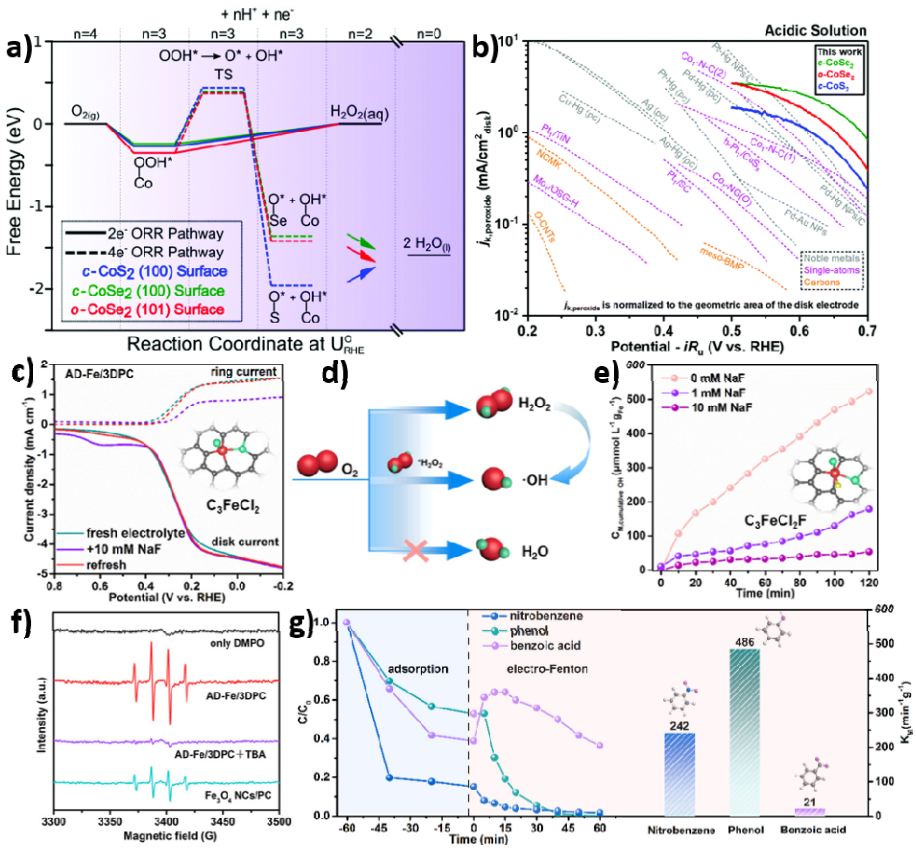

Fig. 4. (a) Calculated free energy diagrams of 2e⁻ and 4e⁻ ORR for c-CoS_2 (100) (blue), c-$CoSe_2$ (100) (green), and o-$CoSe_2$ (101) (red). (b) Kinetic current density for H_2O_2 normalized to geometric surface area and compared to previously reported 2e⁻ ORR catalysts. (a,b) Reproduced with permission from Ref. [74]. Copyright 2020, Royal Chemistry Society. (c) Linear sweep voltammetry (LSV) with 1200 r/min rotation and 10 mV s^{-1} scan rate in 0.05 mol/L Na_2SO_4 (pH = 6) for fresh electrolyte (green), 10 mmol/L NaF poisoning agent (purple), and repeated with fresh electrolyte after poisoning measurements (red). (d) Schematic representation of O_2 stepwise reduction to H_2O_2 and OH•. (e) OH• yield with increased levels of poisoning agent, NaF. (f) Spin trapping ESR spectra with DMPO (3 mmol/L). (g) degradation of nitrobenzene (blue), phenol (green), and benzoic acid (purple with calculated kinetic constants normalized to Fe mass (K_M). (c–g) Reproduced with permission from Ref. [76]. Copyright 2020, Springer Science.

drogen bonding network of melamine and cyanuric acid before dropping out of the solution as a precipitate. GO was then added into the solution to form a composite. The precipitate was freeze-dried and carbonized to produce high-loading copper single atoms in nitrogen-doped graphene (Cu-SA/NGO). The atomic dispersion of Cu was visualized in HAADF-STEM measurements, and EXAFS studies showed a Cu-N coordination number of 4.0, signifying the formation of CuN_4 moieties. The electro-Fenton activity of the obtained samples was then tested towards the degradation of various organic contaminants, such as acetaminophen (APAP), in the presence of H_2O_2 at controlled concentrations. Complete electro-Fenton degradation of APAP (10 mg L^{-1}) was achieved within 1 h at a catalyst loading of 25 mg L^{-1}. First principles DFT calculations suggested that the mechanism involved a two-electron transfer step to form H_2O_2 followed by a third electron transfer and homolytic fission of H_2O_2 to produce HO•, which was confirmed in ESR measurements in the presence of a spin-trapping agent, 5,5-dimethyl-1-pyrroline N-oxide (DMPO), and methanol as a hydroxyl radical quenching agent.

One step beyond the progress by Wu *et al.* [76] would be to develop a bifunctional catalyst that can facilitate both the electrochemical production of H_2O_2 and homolytic cleavage of H_2O_2 to HO•. This is demonstrated recently by Cao and co-workers [77], where they synthesized single iron atoms on porous carbon with Fe-C/Fe-Cl in an unsaturated coordination configuration through a three-step synthesis route. Experimentally, $FeCl_3$, p-phthalic acid (PTA), and NaOH were mixed and subject to a hydrothermal treatment to produce a hydrogel mixture, which was washed and dried before carbonization and finally acid treatment to remove undesired metal particles. The unique Fe-C/Fe-Cl coordination environment was confirmed by EXAFS measurements. Electrochemical studies (Fig. 4(c)) confirmed a 3e⁻ ORR pathway with H_2O_2 formed as an intermediate and an additional electron transfer to the produced H_2O_2 generating HO•. A schematic representation of this reaction pathway is depicted in Fig. 4(d), and results from DFT calculations suggest that the unique Fe coordination configuration was responsible for the 3e⁻ ORR pathway. Notably, in RRDE collection experiments (Fig. 4(c)), a clear increase in ring current was observed upon the removal of the poisoning agent NaF, as F^- was known to attach to the Fe single atom sites within the material, blocking O_2 adsorption and preventing oxygen reduction from occurring (Fig. 4(e)). The formation of HO• was, again, confirmed by ESR measurements using DMPO as the spin trapping agent and *tert*-butyl alcohol (TBA) as the

HO• quenching probe (Fig. 4(f)). The electrocatalyst was further applied to the degradation of small molecules (Fig. 4(g)), where complete degradation of phenol and nitrobenzene (at an initial contaminant concentration of 0.12 mmol/L) was achieved in 45 min at an applied potential of 0.15 V *vs*. RHE. The degradation rate for benzoic acid was markedly lower, which was correlated to the difference in aromatic ring electron density and the consequent catalyst-adsorbate interactions.

In summary, HO• can be generated from the partial reduction of oxygen or the partial oxidation of water as seen with H_2O_2. HO• can also be formed by the homolytic fission of H_2O_2 and possesses the highest oxidizing power of the three ROS discussed. Rational design and engineering of the electrocatalysts is critical in dictating the specific reaction pathways, efficiency and selectivity. Table S2 summarizes the performance of additional electrocatalysts for HO• generation in recent literature.

2.2. Reactive chlorine species

Another category of RS is the RCS, which are particularly important to keep in mind when chloride-containing electrolytes are utilized, especially under oxidizing conditions [78–82]. Chlorine evolution reaction (CER, E^0 = 1.358 V *vs*. RHE), shown in Reaction (11), is energetically more favorable than WOR in aqueous electrolytes.

$$2Cl^- \rightarrow Cl_2 + 2e^- \quad (11)$$

$$½Cl_2 + H_2O \rightarrow HClO + H^+ + e^- \quad (12)$$

$$Cl^- + H_2O \rightarrow HClO + H^+ + 2e^- \quad (13)$$

$$6ClO^- + 3H_2O \rightarrow 2ClO_3^- + 6H^+ + 4Cl^- + 3/2O_2 + 6e^- \quad (14)$$

Note that chlorine produced in aqueous media can undergo hydrolysis forming hypochlorous acid (HClO, Reactions (12,13)), which partially dissociates to hypochlorite ion (ClO^-), a species that can be further oxidized to chlorate (ClO_3^-, Reaction (14)). Further oxidation of ClO_3^- can lead to the formation of perchlorate (ClO_4^-). ClO_3^- and ClO_4^- are toxic, stable byproducts that should be considered [83]. This activity has been exploited for the design of chlorine-generating electrocatalysts [21,84–92]. For instance, Cho and colleagues [93] developed an unique composite material containing $Ir_{0.7}Ta_{0.3}O_y/Bi_xTi_{1-x}O_z$ heterojunctions as an anode catalyst for electrochemical chlorine generation, where the outer layer of $Bi_xTi_{1-x}O_z$ served to improve OH^* adsorption, while the inner $Ir_{0.7}Ta_{0.3}O_y$ layer improved electrical conductivity and electron shuttling. Similar mixed metal oxide materials have also been implemented in previous studies as some of the most efficient RCS generating electrocatalysts [94,95]. The sample was synthesized by following a thermal decomposition approach in which H_2IrCl_6 and $TaCl_5$ were coated on Ti metal sheets and annealed at 525 °C. The heterojunctions were created through the deposition of bismuth citrate and titanium butoxide solutions followed by a secondary annealing step at 425 °C. LSV of the resulting material was performed in NaCl (50 mmol/L), and the RCS current efficiency (η_{RCS}) was calculated by Eq. (15),

$$\eta_{RCS} = (2VF/I)(d[Cl_{DPD}/dt] \quad (15)$$

with V being the electrolyte volume (L), F the Faraday's constant (96480 C mol^{-1}), $[Cl_{DPD}]$ the RCS concentration (mol/L), I the current (A), and t the electrolysis time (s). The $Ir_{0.7}Ta_{0.3}O_y$ catalyst layer proved essential for sufficient electrical conductivity, while a decreasing Bi:Ti molar ratio resulted in improved RCS generation. Note that the electrochemical oxidation of chloride can follow two reaction pathways on a metal oxide surface, as shown in Reactions (16,17).

$$MO_x(HO•) + Cl^- \rightarrow MO_x + ½Cl_2 + OH^- \quad (16)$$

$$MO_{x+1} + Cl^- \rightarrow MO_x + ClO^- \quad (17)$$

Reaction (16) depicts the formation of hydroxyl radicals on metal oxide surfaces (MO_x) followed by a fast direct electron transfer from Cl^- to produce Cl_2, which then undergoes hydrolysis forming hypochlorous acid through Reaction (17), depicting the direct transfer and consumption of oxygen within the metal oxide lattice forming the conjugate base of hypochlorous acid (ClO^-). Reaction (16) occurs much faster than displacement of the lattice oxygen, which makes this reaction pathway more desirable for electrochemical chlorine generation [96]. In the study of the degradation kinetics of formate ions, it was determined that high Bi mole fractions (> 0.3) accelerated RCS generation through the undesirable pathway of Reaction (17); however, a low mole fraction of Bi (≤ 0.3) resulted in improved chlorine generation with η_{RSC} > 85%. Recently, Hong and colleagues [86] prepared a similar composite anode material for RCS generation and also determined that Bi incorporation had limited to adverse contributions toward catalysis.

Other researchers came to similar conclusions that TiO_2 may serve as a sole framework for RCS generation. For instance, Heo and co-workers [85] recently used RuO_2 deposited on black TiO_2 (b-TiO_2) for CER electrocatalysis. b-TiO_2 was synthesized through electrochemical anodization of a Ti foil followed by an annealing step at 450 °C in an argon atmosphere, which resulted in the formation of significant oxygen vacancies within the TiO_2 lattice, enhanced visible light absorption and hence a blackened coloration. A crystalline TiO_2 sample was created for comparison in air and denoted (c-TiO_2). RuO_2 nanoparticles were deposited on the resulting titania through a pulsed electrodeposition method using solution-phase Ru^{3+}. HAADF-STEM and XPS measurements confirmed the homogeneous deposition of RuO_2 nanoparticles on the titania scaffolds. Dramatic differences were seen in the CER polarization curves in which RuO_2/b-TiO_2 displayed excellent CER activity with an η_{RSC} of 95.25% in 5.0 mol/L NaCl, in comparison to almost 0% with RuO_2/c-TiO_2. Mott-Schottky analysis showed that RuO_2/b-TiO_2 exhibited a charge carrier density 5 orders of magnitude higher than that of RuO_2/c-TiO_2. Furthermore, cyclic voltammetry measurements in the presence of ferrocene revealed that RuO_2/c-TiO_2 was electrochemically inactive under anodic polarization. Therefore, the remarkable CER performance of RuO_2/b-TiO_2 was attributed to the improved conductivity of the b-TiO_2 scaffold under anodic conditions.

In another study, Ha and co-workers [84] prepared metal oxide catalysts for highly selective chlorine generation by using a hot injection method to synthesize Co_3O_4 nanoparticles (Co_3O_4 NPs) with cobalt(II) acetate and myristic acid as the precursors in 1-octadecene at 315 °C. Amorphous CoO_x (Co-Pi), bulk CoO, and bulk C_3O_4 were also prepared by electrodeposi-

tion, along with commercially available dimensionally stable anode (DSA) composed of RuO_2-based mixed-metal oxides used for comparison. The structure of the Co_3O_4 NPs was carefully examined by XRD, TEM, and XPS measurements, and spin-coated on FTO for electrochemical assessments. From Fig. 5(a), one can see that the Co_3O_4 NPs exhibited a more positive onset potential towards CER than bulk CoO and Co_3O_4 in 0.6 mol/L NaCl. *In situ* X-ray absorption near-edge structure (XANES) measurements were carried out under CER and OER conditions to discern possible competition between the two pathways. From Fig. 5(b), one can see that under OER conditions, the XANES profile exhibited an apparent positive energy shift, as compared to that under CER, signifying a higher Co oxidation state in the former. This suggests that under CER conditions O_2 did not compete with Cl^- for Co binding. It was therefore determined that the reaction mechanism did not follow the classical metal oxide pathway, as described in Reactions (16) and (17), but the one proposed by Krishtalik [97]. In the Krishtalik pathway, the chlorine adsorbate binds to the metal of the metal oxide (*e.g.*, Co in the present study) followed by two electron-transfer steps from Cl to the metal center, such that a cationic chlorine intermediate is produced and then combined with Cl^- to form the final Cl_2 product (Fig. 5(e)), where the rate determining step is the second electron-transfer process. This is supported by results from *in situ* Raman spectroscopy measurements, where the Co–Cl vibration (ca. 502 cm^{-1}) became intensified with an anodic shift of the applied potential (Fig. 5(c)), whereas the Raman shift remained virtually invariant in H_2O, D_2O, and $H_2{}^{18}O$ (Fig. 5(d)), ruling out any possible contribution of H or O to the interaction.

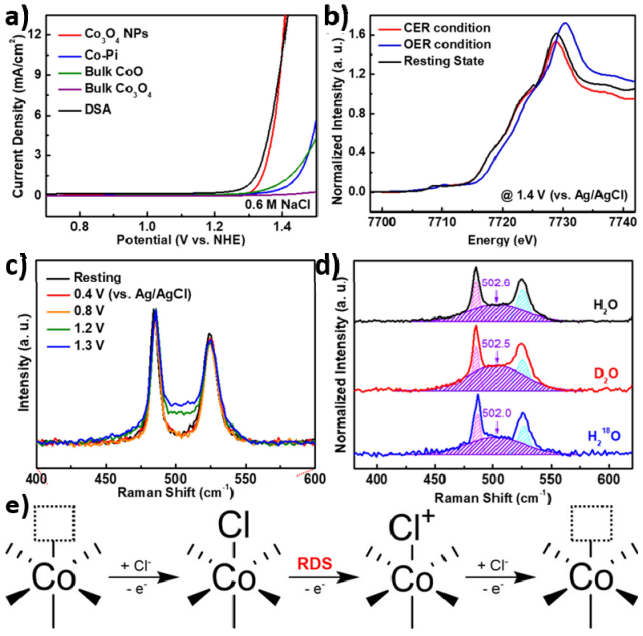

Fig. 5. (a) Polarization curves for chlorine evolution reaction (CER) for various cobalt containing materials. (b) *In situ* XANES at Co K edge for Co_3O_4 nanoparticles under CER and OER conditions in 0.6 mol/L NaCl and 0.5 mol/L phosphate buffered species (Pi), respectively. (c) *In situ* Raman measurements under increasing oxidative potentials from 0.4 to 1.3 V in 4 mol/L NaCl. (d) Broad peak occurs near 500 cm^{-1} ascribed to Co–Cl, with deconvolution in H_2O, D_2O, and $H_2{}^{18}O$. Reproduced with permission from ref. [84]. Copyright 2019, American Chemical Society.

RCS can also be produced using nonactive electrode materials including DSA. For example, Araujo and co-workers [98] compared the use of two DSA materials (IrO_2 and RuO_2) and BDD toward inactivation of *Pseudomonas aeruginosa*, a gram-negative bacterium commonly found in water and soil. With a stainless-steel cathode and a 7 mmol/L Na_2SO_4 electrolyte, complete inactivation of 100 mL of 10^6 CFU mL^{-1} bacteria was achieved at a current density of 33.3 mA cm^{-2} within 30 min for both DSAs, in comparison to 60 min for BDD. Most interestingly, complete activation using the DSAs was achieved in just 5 min under the same experimental conditions and the addition of 1 mmol/L NaCl. BDD inactivation time also improved with the addition of NaCl to 30 min. *N*,*N*-diethyl-*p*-phenylenediamine (DPD) was used as a colorimetric method to quantify RCS produced during electrocatalysis. These measurements suggested RuO_2 to be the most active of the three materials toward RCS generation producing more than 5 mg L^{-1} of active chlorine within 15 min of electrolysis. These results highlight the ability for nonactive electrodes such as BDD and other DSAs to produce RCS under electrochemical conditions.

In summary, the generation of RCS is important when the electrolyte or water used for disinfection contains a significant concentration of chloride ions. Chlorine can be produced from the oxidation of chloride ions, and further oxidation can produce various RCS including hypochlorous acid, chlorate, and perchlorate. If the disinfected water is to be consumed by humans, it would be important to prevent the formation of toxic stable species such as chlorate and perchlorate. Table S3 summarizes the performance of additional electrocatalysts for the generation of RCS reported in recent studies. Beyond chloride, the presence of other species in the disinfection medium gives rise to the formation of other RS discussed in the following section, such as reactive nitrogen and sulfur species.

2.3. Other reactive species

Under typical electrochemical conditions, ROS and RCS are the primary RS that are produced. However, depending on the specific experimental conditions, the production of less common RS, such as RNS [99–101] and RSS [102–105], need to be investigated as well. A series of possible reaction pathways toward RNS is provided in equation (18).

$$NO_3^- \leftrightarrows NO_2^{\bullet} \leftrightarrows NO_2^- \leftrightarrows NO^{\bullet} \leftrightarrows HNO \leftrightarrows NR_{3-x}H_x \quad (18)$$

RNS can be produced through nitrate (NO_3^-) reduction (from left to right in Reaction (18)), or by amine ($NR_{3-x}H_x$) oxidation (from right to left in Reaction (18)). A variety of amine species may be present in the experimental systems, including ammonia (NH_3) and biologically derived amines, such as nitrogen within the amino acid L-arginine [106]. Through these reduction or oxidation reactions, a range of RNS can be produced, including nitrogen dioxide ($N_2O^{\bullet}$), nitrite (NO_2^-), nitric oxide ($NO^{\bullet}$), and nitroxyl (HNO) [107]. Many more species can be formed between HNO and ammonia, including nitroxyl radical (H_2NO) and hydroxyl amine (H_2NOH) [108]. These various RNS are often grouped together and referred to as NO_x in the litera-

ture [109–112]. It is also important to note that formation of these RNS require either molecular oxygen or water. Therefore, these species should be considered during electrocatalysis when nitrogen-containing compounds are present within the system of interest.

Like RNS, RSS can be found in many oxidation states and are often grouped together as SO_x species [102]. Non-oxygen containing RSS can be formed by the reduction of elemental sulfur (S_2) or oxidation of sulfide-type species, like hydrogen sulfide (H_2S), as seen in Reaction (19).

$$H_2S \leftrightarrows HS^{\bullet} \leftrightarrows H_2S_2 \leftrightarrows S_2^{\bullet} \leftrightarrows S_2 \quad (19)$$

Such non-oxygen containing RSS include thiyl radical ($HS^{\bullet}$), hydrogen persulfide (H_2S_2), and persulfide radical ($S_2^{\bullet-}$) [103]. The importance of RSS, as compared to RNS and ROS, has been a growing topic in biology, and it has been concluded that biologically derived RSS play a more important role in oxidative stress than once believed nearly two decades prior [103–105]. For these reasons, RSS should be taken into account in electrochemical systems containing elemental sulfur, hydrogen sulfide, or sulfate species.

Other peroxo species may be formed under electrochemical conditions beyond hydrogen peroxide, such as persulfate, percarbonate, and perphosphate [113–117]. Specifically, persulfate (SO_5^{2-} or $S_2O_8^{2-}$) can be produced from sulfate, percarbonate (H_3CO_6) from carbonate, and perphosphate (PO_5^{3-} or $P_2O_8^{2-}$) from phosphate.

Recently, there has also been significant advancement in the electrochemical production of ozone as a viable oxidant source [118–122]. This is a desirable strategy since the production and use of ozone involves only oxygen, preventing the further formation of undesirable byproducts and toxins.

In summary, there are numerous other reactive species, such as RNS and RSS, that can be formed during the electrocatalytic generation of ROS and RCS depending on the disinfection media and precursors. Thus, contributions from these various RS to the electrodisinfection activity cannot be ignored, and careful analysis is necessary.

2.4. Homogeneous electrocatalysis for RS generation

In the above sections, the electrogeneration of RS is primarily achieved by heterogeneous catalysis. However, it should be noted that homogeneous electrocatalysis has also been exploited for RS production [123–128]. For example, Siu et al. [123] recently reviewed their work on redox-active molecular catalysts, and discussed in detail the electrocatalytic mechanisms of radical formation and the activity in the heterodifunctionalization of alkenes. One can imagine the application of a similar homogeneous catalyst for the purposes of microbial control, as these materials produce high-energy radical species which can be used for the deterioration of microorganism components, such as lipids, proteins, and DNA, as described in the sections below.

3. Interactions of reactive species with microorganisms

Now that we have established a foundation to produce RS, it is critical to investigate how these RS interact with microorganisms. RS can cause severe damage within a microorganism at high enough levels and in the absence of remediation pathways [28,129–132]. For instance, RS can oxidize amino acids within proteins and nucleic acids within DNA, leading to protein and DNA inactivation [133–137]. Oxidation of polyunsaturated lipids within the microorganism's lipid membrane can cause structural damage leading to apoptosis and cell death after prolonged lipid membrane degradation [138–142]. Outer lipid membrane degradation is of particular importance since RS do not need to penetrate the cell to cause microorganism inactivation, considering the limited lifespan of the generated RS and difficulties penetrating microbial membranes [143,144]. If the RS can contact the surface lipid layer of the microorganism, microbial inactivation can occur [145,146]. Notably, microorganisms produce small levels of RS on their own, which has led to the development of specific enzymes used to break down RS, as shown in Fig. 6. The following section will explore the regulation of these RS within the cell.

3.1. Oxidative homeostasis regulated within microorganisms

Microorganisms encounter some level of RS regularly with response pathways designed to circumvent the damaging effects of RS [147,148]. Toxic RS can be removed by antioxidant enzymes within a microorganism. These enzymes include superoxidase dismutase (SOD), catalase (Cat) and glutathione peroxidase (GPx), amng others (Fig. 6) [149]. SOD was first discovered by Fridovich *et al.* [150] in 1969. The most common RS found natively within the cell is $O_2^{\bullet-}$ produced within the electron transport chain of mitochondria [9,12]. SOD has been found to catalyze the conversion of $O_2^{\bullet-}$ to H_2O_2. Working alone, the conversion of one RS to another is not ideal; however, Loew identified an antioxidant enzyme, Cat, in 1900 which catalyzed the conversion of H_2O_2 to H_2O and O_2 [151]. In 1957, Mills [152] discovered another enzyme, GPx, that was responsible for

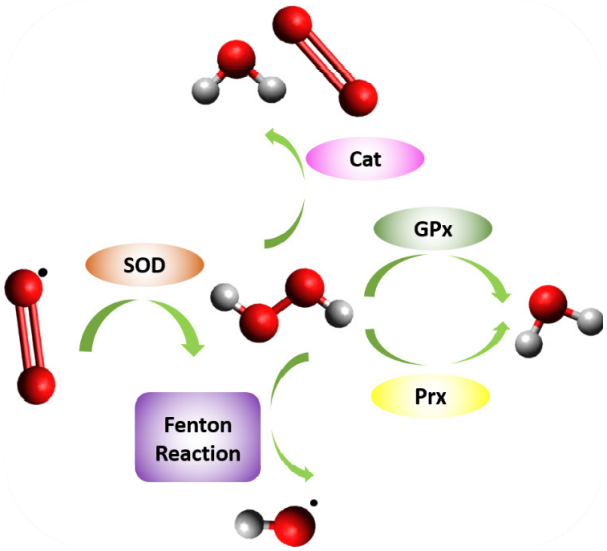

Fig. 6. Regulation of reactive oxygen species within the cell by enzymes SOD, Cat, and other peroxidase enzymes (GPx and Prx). Red spheres represent oxygen and grey spheres denote hydrogen.

breaking down hydroperoxides, including lipid hydroperoxides, which were formed during radical reactions with lipid membranes found in microorganisms. There have been several other peroxidase (Prx)-like enzymes discovered thereafter [4,153–156]. A schematic summary of RS conversion within the cell is shown in Fig. 6. It is important to note the familiarity that microorganisms have with RS, such as $O_2^{\bullet-}$ and H_2O_2, due to their production within mitochondria and their evolved methods for controlling damage from these species. RS including $HO^{\bullet}$ and HClO are not directly produced within the cell, providing less pathways for damage prevention by the microorganism's stress response. Under increased levels of oxidative stress, microorganisms are unable to prevent damage caused by their interaction with RS. In these cases, there are some measures that the microorganism can take to repair damage to the cell. In-depth studies of these pathways can be found in the literature [156–159].

Microorganisms exist under a spectrum of RS exposure (Fig. 7(a)). This is because microorganisms naturally produce some level of RS, most often within mitochondria, through aerobic respiration processes. Normal levels of RS are handled by various cellular processes and minor damage caused by RS can be repaired. When a certain RS threshold is surpassed, cellular processes cannot keep up with RS removal and the microorganism enters a state of oxidative stress. Under these conditions, microbes increase the production of glutathione (GSH), which is limited by the availability of the precursor amino acid, cysteine, and the expression of the gene *gshA* [160]. GSH will become oxidized to glutathione disulfide (GSSG) upon contact with RS (Fig. 7(b)). Oxidation of GSH prevents oxidation of other nearby species that may result in long-lasting damage to the microbial organism. Many research reports have used this as a method of determining effective antimicrobial catalysts through quantifying GSH interactions [161,162]. Electrocatalysts must produce enough RS to overcome the presence of glutathione before moving on to degrade the microorganism's cellular components. One frequently used method for quantifying GSH and thiol oxidation is known as the Ellman's assay [163,164]. In this process the Ellman reagent, 5,5′-dithio-bis(2-nitrobenzoic acid) (DTNB), is added and light absorption near 430 nm is measured over time (Fig. 7(c)). As shown in Fig. 7(a), there is a point at which the microorganism cannot properly function in the presence of RS, and experience damaging effects, as detailed below.

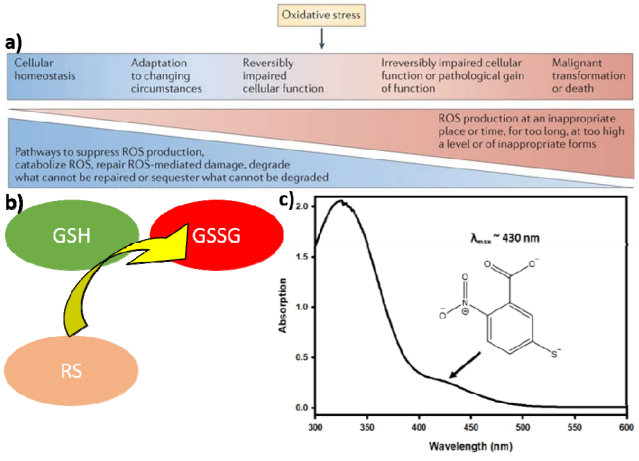

Fig. 7. (a) Spectrum of cellular response to RS ranging from cellular homeostasis, left, to cell death, right. (b) Schematic representation of GSH oxidation to GSSG by RS. (c) UV-vis absorption spectrum for the Ellman's reagent. (a) Reproduced with permission from Ref. [147]. Copyright 2013, Springer Nature. (c) Reproduced with permission from Ref. [163]. Copyright 2020, Royal chemistry society.

3.2. Damaging effects caused by reactive species

3.2.1. Lipids

Exogenous RS first encounter the lipid membrane of the cell, and this must be breached to further interact with organelle and other cell components, such as proteins and DNA. In eukaryotes, this lipid membrane is composed of glycerophospholipids with > 50% of these phospholipids comprised of phosphatidylcholine [165]. These lipids self-organize to form a bilayer exposing polar groups toward the surface of the membrane. Nonpolar groups within the membrane are comprised of saturated and cis-unsaturated fatty acyl chains. Both the polar groups at the surface of the membrane and the unsaturated acyl chains are vulnerable to RS oxidation. The oxidation of the unsaturated nonpolar fatty acyl chains by RS is known as lipid peroxidation and results in oxidative degradation [145,146,166–168]. Fig. 8(a) depicts the lipid peroxidation of linoleate resulting in structural changes to the lipid and addition of polar oxygen-containing functional groups. This reaction follows a free radical chain reaction mechanism resulting in proliferation of membrane damage and incorporation of oxygen functional groups within the nonpolar chains. The oxygen functional groups at this site are polar in nature and leads to increased hydrophilicity and ultimately decomposition of the membrane barrier and exposure of endogenous cellular components.

3.2.2. Proteins

Once the lipid membrane of the organism is compromised, further RS damage may be accrued to inner cellular components, including proteins and DNA. Exposure of RS to a protein leads to modifications of amino acid side chains by protein oxidation. These changes can prevent protein function or make the protein increasingly susceptible to proteolytic degradation by the proteosome, a catalytic ATP-independent enzyme complex designed to degrade proteins tagged by ubiquitin [169]. This is part of the cell's evolved methods for self-preservation by removing damaged cellular components.

The ability for the proteosome to track and remove damaged protein has been shown to correlate with oxidant concentration [170]. At mild oxidant concentrations the proteosome can keep up with proper removal of damaged proteins. Under conditions of high oxidant concentrations, damaged proteins are less likely to be captured and removed from the cell matrix resulting in an increased opportunity for these proteins to become further damaged or interact with undamaged cell components. These protein-protein interactions can lead to protein cross-linkage where two proteins become attached to one another either by hydrophobic, electrostatic, or covalent interac-

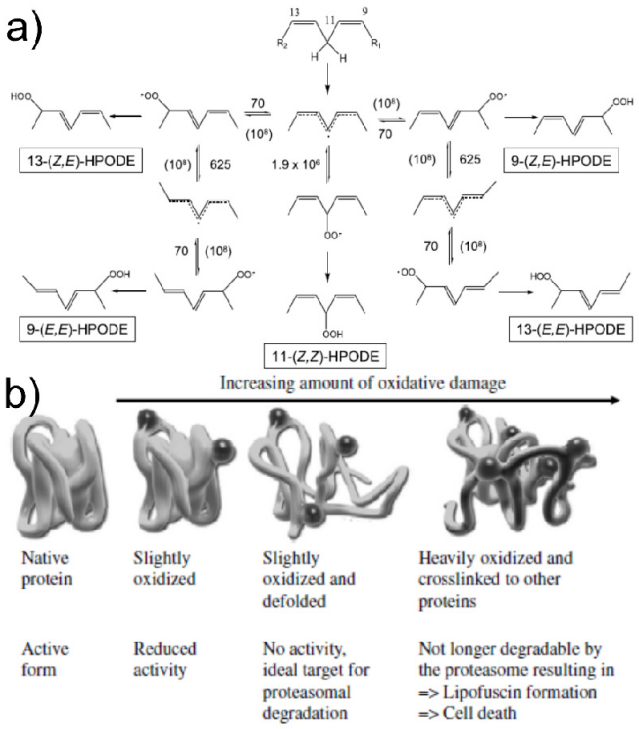

Fig. 8. (a) An example of lipid peroxidation using linoleate as the starting substrate. Reproduced with permission from Ref. [167]. Copyright 2005, Elsevier. (b) Results of protein damage caused by increased levels of oxidation. Reproduced with permission from Ref. [170]. Copyright 2003, Elsevier.

tions. Left unchecked, the cross-linking can continue and create a protein aggregate. Such aggregates can overwhelm the proteolytic system making basic cell function increasingly difficult. Fig. 8(b) depicts the progression of protein damage with increased oxidation from left to right. Heavily oxidized and cross-linked proteins cannot be degraded by the proteosome and establish cell signals related to programmed cell death. For antimicrobial purposes, this creates a circumstance in which increased RS production only improves bacterial inactivation efficiency.

3.2.3. DNA

A third vital component susceptible to RS interactions is DNA. The central dogma of biology states that DNA holds the code necessary for producing cellular components critical for survival. DNA is converted to RNA through transcription within the nucleus and RNA produces the final product including proteins and enzymes through translation [171]. Thus, cell function relies on the preservation of DNA and any deletions, mutations, or other structural damage can lead to devastating effects during the transcription or translation processes.

Structurally DNA is comprised of a sugar phosphate backbone connected in a double helix through hydrogen bonding between 4 unique nucleotide bases, adenine, thymine, guanine, and cytosine. Damage to the DNA can occur in many ways including deletion of one or more nucleotide base pair, mutation of one or more base pairs replaced by another, or by breaks in the DNA chain either through single (SSB) or double strand breaks (DSB) [172,173]. This type of damage to DNA is so frequent that multiple recovery pathways have evolved within the cell to correct such damage and prevent mutant RNA or protein from being produced. With this reasoning, DNA damage does not directly result in cell death, but prolonged exposure to RS and further DNA damage can result in irreversible DNA damage and contribute to cell inactivation.

OH• has been shown to interact with DNA nucleotide base pairs through addition to the pyrimidine region of thymine and cytosine and to the purine region of adenine and guanine [174]. This interaction can lead to separation of the double stranded structure and prevent transcription from occurring. HClO has also been shown to cause nucleotide chlorination leading to similar damaging effects [175]. With sufficient RS concentration the microorganism exhibits an increase in devastating effects including lipid peroxidation, protein degradation, and irreversible DNA damage culminating to prevent necessary cell functions and ultimately resulting in cell inactivation.

4. Electrogenerated reactive species for microbial inactivation

Now that we have established a foundation for different types of RS and their interactions with microorganisms, it is of particular interest to summarize where the field of electrogenerated RS for microbial inactivation currently resides. Electrogenerated RS for microorganism inactivation is a new and growing field. In the studies of electrodisinfection throughout the last decade [31,176–194], the electrochemical activity is primarily attributed to electric field (EF), microbial cohesion, and electrocoagulation, with less focus on quantifying RS generation and the impacts on microbial inactivation. RCS are the leading RS quantified and discussed in these accounts [177,179–181,189,192,193,195]. For instance, Cotallis [195] and colleagues recently reported on a water electrodisinfection device created with a stainless-steel cathode and a BDD anode attached by a filter pressed stack with 40 mm separation between the cathode and anode compartments. Three of these filter stacks were used in series during experimental operation. Chloride (82.19 mg dm^{-3}), nitrate (14.8 mg L^{-1}), sulfate (152.10 mg L^{-1}), ammonia (18.89 mg L^{-1}), and *E. coli* (1100 – 2200 CFU mL^{-1}) were the most likely species within the untreated water to interact with the electrode surface during water electrodisinfection. An optimized current density in the range of 5–10 mA m^{-2} and applied electrical charge of 0.1 kAh L^{-1} resulted in complete disinfection of the contaminated water. Successful removal of *E. coli* was quantified through changes in water turbidity and cell cultures of the resulting water. Free and combined chlorine species were considered as the primary disinfectants, and ion chromatography measurements showed a level close to 0.5 mmol/L at the applied current density of 10 mA m^{-2} and electrical charge of 0.1 kAh L^{-1}. It was noted that some leaching of Fe occurred at the stainless-steel anode and these dissolved species might have assisted, to some degree, in the coagulation process and decreased water turbidity.

Other research groups have also had success studying simulated wastewater, created under controlled laboratory condi-

tions. This allows for close studies into the possible reactants involved and possible products generated during the electrodisinfection process. Ding and colleagues [192] used a commercially available DSA electrode composed of Ru-Ir-Ti oxides with graphite felt as a cathode material, and studied how changing water conditions would influence wastewater treatment. Simulated wastewater was created using deionized water, NaCl, and NH_4Cl (as a source of ammonia), and electrodisinfection rates were measured at varying contents of ammonia (0, 10 mg L^{-1}) and chloride (50–500 mg L^{-1}), as well as constant *E. coli* concentration (1000 CFU mL^{-1}). It was determined that bacterial inactivation was optimized at 250 mg L^{-1} chloride ions, and addition of more chloride ions did not improve bacterial inactivation under the same reaction conditions. Also, a minimum applied charge of 0.07 Ah L^{-1} was required for complete water disinfection over a 24 h period. Free chlorine generation was found to vary with the applied electrical charge and peaked at 0.4 Ah L^{-1}. Beyond this applied charge, chloramines and chlorate ions were the leading chlorine species produced. Complete *E. coli* removal was obtained at 0.07 Ah L^{-1}, 250 mg L^{-1} chloride, in 4 h.

As Ghernaout *et al*. [177] pointed out in their most recent review, future work must also look to determine contributions from oxygen containing RS including the hydroxyl radical. In fact, ROS have been identified under similar electrochemical conditions without the presence of chloride in the electrolyte solution. For example, Qi and co-workers [196] observed synergistic effects between rGO and BDD toward electrochemical inactivation of *E. coli*. Experimentally, GO was first synthesized by a modified Hummer's method and chemically reduced by hydrazine to produce rGO. The electrodisinfection tests were carried out with an electrochemical cell comprised of a 400 mL beaker, commercially purchased BDD anode (4 cm^2), and a stainless-steel cathode (4 cm^2) separated 1 cm away from the anode. Multiple electrochemical measurements were conducted with rGO alone, BDD alone, and with both BDD and rGO. It should be noted that rGO was dispersed in the electrolyte during these studies. It was found that increasing the applied current density led to improved antimicrobial activity. rGO loading, degree of reduction, and electrolyte concentration were then optimized to further improve the antimicrobial activity. The HO• concentration was quantified by a colorimetric method involving reaction with *N*,*N*-dimethy-*p*-nitrosoaniline. It was observed that the HO concentration increased over electrolysis time and was markedly higher in the presence of both BDD and rGO, as compared to that with BDD or rGO alone. The antimicrobial activity was also significantly better in the presence of BDD and rGO, suggesting that the electrochemically generated HO• was responsible for the antibacterial performance, where rGO was postulated to increase the electric field within the electrolyte and improve charge carrier migration, leading to improved antimicrobial inactivation by direct charge transfer. However, when the power was turned off after 5 min's electrolysis, the *E. coli* count continued to decline over time. This implies that in addition to RS, other contributors need to be identified and considered for the continued bacterial inactivation, and more systematic research is desired. A similar electrochemical setup was also utilized in other reports in the investigation of pristine TiO_2 and bismuth-doped TiO_2 nanotubes [197,198].

A significant amount of research has also been dedicated to the study of BDD toward water disinfection over the previous two decades [51,57,183,193,195,196,199–205]. BDD is typically produced through chemical vapor deposition at low temperatures often with methane as a carbon source and gaseous boron in the form of B_2H_6 or $B(OCH_3)_3$ [206]. Pristine BDD contains only sp^3 carbon similar to diamond; however, sp^2 type surface carbon defects are widely accepted as active sites for much of the catalytic properties associated with the BDD electrodes [204,207]. With this reasoning, significant research has been developed toward the preparation of nanocrystalline diamond (NCD), containing crystal grain sizes under 100 nm, and ultra-nanocrystalline diamond (UNCD), containing grain sizes of 3–5 nm [208,209]. Reducing the BDD grain size introduces surface defects and sp^2 carbon content thereby improving electrochemical performance.

For example, Glass and co-workers recently studied the production of H_2O_2 using an UNCD BDD electrode [205]. Commercially available boron-doped UNCD was deposited onto a silicon wafer by a thin copper wire and silver paste. The copper wire and paste were isolated from the electrolyte by glass tubing and nonconductive epoxy. XPS was used to identify functional groups on the surface of the UNCD electrode both before and after electrochemical cycling. It was found that prolonged use of the electrode under cathodic conditions resulted in removal of oxygen functional groups at the electrode surface and decreased H_2O_2 production. In addition, H_2O_2 generation could be improved by a pre-anodization step in which the UNCD electrode was first oxidized prior to cathodic H_2O_2 generation. Furthermore, the use of a repeated oxidation-reduction cycling process was found to improve H_2O_2 generation under catholic conditions and prolong the electrode lifetime. Incorporation of an oxidation step allowed reincorporation of oxygen functional groups on the surface of the electrode necessary for H_2O_2 generation.

In a later study, Glass and co-workers [210] demonstrated the effectiveness of the potential cycling process toward blackwater disinfection using an oxidized BDD electrode. The potential cycling approach improved the disinfection energy efficiency by as much as 124%. Furthermore, the production of RCS was quantitatively assessed using black water samples containing 0.154 mol/L NaCl. Potential cycling (between −2 and +2 V) was shown to dramatically improve the production of free Cl_2 to 30 μg cm^{-2}, as compared to less than 15 μg cm^{-2} produced by constant applied potentials of +2 and −2 V. Mechanistically, Cl^- adsorption and oxidation was facilitated by anodic polarization due to the generated HO• species, and cathodic polarization led to desorption of RCS into the bulk solution. Similarly, O_2 rather than Cl^- was adsorbed during the anodic cycles to produce H_2O_2. This demonstrates how multiple RS were produced under working conditions, each contributing to the disinfection of blackwater.

In another study, Jiang *et al*. [211] incorporated a membrane to separate the cathode and anode compartments in

their study of transition-metal (TM) SACs toward oxygen reduction for hydrogen peroxide generation and their applications in bacterial inactivation. They used a cathode material for hydrogen peroxide production and a commercial IrO_2 catalyst as the anode, and the anode and cathode compartments were separated by a Fumasep FAA-3-PK-130 anion exchange membrane in an H cell. Various TMs (i.e., Fe, Pd, Co, and Mn) were atomically deposited on carbon nanotubes (CNT) synthesized by a freeze-drying and thermal annealing process under an Ar atmosphere at 600 °C. Fig. 9(a) shows the HAADF-STEM image of Fe-CNT where Fe single atoms can be readily identified. Consistent results were obtained in the corresponding FT-EXAFS spectrum (Fig. 9(b)), where no evident Fe-Fe neighbors can be found; for bulk Fe_3O_4 (blue) and Fe foil (black), the Fe spectra exhibited a small peak characteristic of Fe-O linkage. Electrochemical tests revealed a H_2O_2 yield over 80% for the Fe-CNT sample within a wide range of applied potentials, which decreased in the order of Fe-CNT > Pd-CNT > Co-CNT > Mn-CNT (Fig. 9(c)). Two additional Fe containing samples were prepared for comparison, one with nitrogen doping (Fe-N-CNT) and the other by a gas-phase reduction step of the as-prepared Fe-CNT, denoted as Red. Fe-CNT. From Fig. 9(d) one can see a significant loss of H_2O_2 production with the addition of N (red) or reduction (blue), likely due to Fe-N propensity toward 4e⁻ ORR and removal of oxygen during the reduction process losing the Fe-C-O character. DFT analysis further supported the proposed F-C-O moiety as the active site for selective H_2O_2 generation with initial O_2 adsorption occurring on the C site. The materials were then tested for electrochemical disinfection of water by quantifying the inactivation of *E. coli* at neutral pH and in a phosphate buffered saline solution (PBS, 0.1 mol/L) at the catalyst loading of 0.5 mg cm^{-2} and applied current density of 20 mA cm^{-2}. Colorimetric analysis showed an H_2O_2 concentration of 1613 ppm after 210 min's electrolysis, with a calculated FE of 90.8%. Apparent inactivation of *E. coli* was observed with the population decreased by 43% in 5 min and 99.9999% in 120 min (Fig. 9(e)).

5. Conclusions and perspectives

In summary, substantial progress has been made toward a fundamental understanding of the electrochemical generation of various RS and their implication in bacterial inactivation. RRDE measurements have proven to be a most popular and trusted route toward the characterization of RS generation, particularly for the two-electron reduction of oxygen producing H_2O_2. Anodic and cathodic pathways are both feasible routes toward electrocatalytic generation of RS with a slight edge given to the cathodic pathways, primarily due to favorable thermodynamics. Among the significant breakthroughs in the field over recent years is the work demonstrating the feasibility of H_2O_2 homolytic fission under electrochemical conditions yielding highly reactive HO• [77]. Furthermore, there have been a number of studies into the practical applications of RS-generating electrocatalysts toward microbial disinfection. These studies have provided the groundwork of research to further understand the conditions required for effective disinfection, in particular, in light of the recent emergence of SACs.

Toward future progress into the field, significant breakthroughs are needed on various fronts. Rational design and engineering of effective electrocatalysts is a critical first step toward electrochemical microbial inactivation. For instance, the breakthrough in the research of monometallic and bimetallic single atom electrocatalysts can be capitalized for the effective and selective production of RS [62,212,213], laying the groundwork to scale up the technology for industrial water disinfection applications. Towards this end, it is important to entail rigorous characterization of a material's electrocatalytic

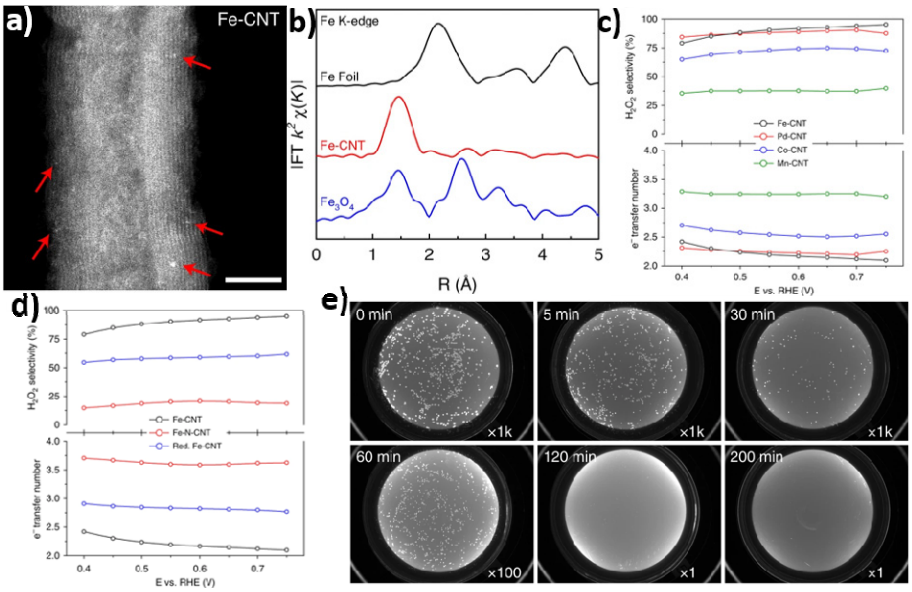

Fig. 9. (a) HAADF-STEM image of Fe-CNT composites. (b) FT-EXAFS R real-space plot of Fe foil (black), Fe-CNT (red), and Fe_3O_4 (blue). (c) Calculated H_2O_2 selectivity and electron transfer number for Fe-CNT (black), Pd-CNT (red), Co-CNT (blue), and Mn-CNT (green). (d) Calculated H_2O_2 selectivity and electron transfer number for Fe-CNT (black), nitrogen doped Fe-N-CNT (red), and gas reduced Red. Fe-CNT (blue). (e) CCD Photos of overnight cultured *E. coli* plates taken from different electrolysis timepoints. Reproduced with permission from Ref. [211]. Copyright 2019, Springer Nature.

capacity toward the generation of RS outlined above, in particular, under *operando* condition. In many cases, more than one RS may provide contributions toward microbial disinfection. It is therefore critical to identify and quantify all possible RS produced within a given system, such that a correlation can be established with the bactericidal activity to advance mechanistic understanding of the inner working of the system of interest.

Furthermore, from the microorganism perspective, current research has focused mostly on a narrow range of possibilities. It is of both fundamental and technological significance to develop electrochemical technologies towards the disinfection of a wide range of microorganisms, including gram-positive/-negative bacteria, viruses, fungi, and helminths, within the context of electrochemical RS generation. For instance, there are three major groups of microorganisms found in wastewater, with the most common being bacteria followed by viruses and helminths [214–219]. It is therefore imperative to quantify a material's ability to inactivate a range of microorganisms to accurately develop an ideal wastewater electrocatalyst. Previous reports have focused primarily on the antibacterial activity toward *E. coli,* the most common gram-negative strain of bacteria, likely due to the accessibility of various *E. coli* strains in most biology laboratories. However, bacterial interactions with electrocatalysts are likely influenced, most likely to a varying degree, by electrostatic interactions with *E. coli*. Future studies should aim to examine and compare the activity to at least one bacterium from each strain, ideally an additional one with gram-positive nature. Furthermore, viruses may pose a higher risk in wastewater than bacteria due to increased difficulty in detection and lower doses required for infection to occur [220,221]. Therefore, future work should also look to quantify disinfection activity toward common virus strains as well. In these studies, it is also critical to carry out relevant assays to unravel the biochemical origin of the disinfection, as various mechanisms of action may be involved, such as oxidative stress induction, protein dysfunction, membrane damage, and transcriptional arrest [222]. Of these, study in conjunction with metabolomic and proteomic analysis [223–225] represents an attractive route and is a focal area of ongoing research.

Note

The authors declare no competing financial interests.

References

[1] D. B. Miklos, C. Remy, M. Jekel, K. G. Linden, J. E. Drewes, U. Hübner, *Water Res.*, **2018**, 139, 118–131.
[2] M. Vallejo, M. F. S. Roman, I. Ortiz, A. Irabien, *Chemosphere*, **2015**, 118, 44–56.
[3] B. K. Sovacool, P. Schmid, A. Stirling, G. Walter, G. MacKerron, *Nat. Energy*, **2020**, 5, 928–935.
[4] J. A. Imlay, *Annu. Rev. Microbiol.*, **2003**, 57, 395–418.
[5] Y. Nosaka, A. Y. Nosaka, *Chem. Rev.*, **2017**, 117, 11302–11336.
[6] K. Krumova, G. Cosa, in: *Singlet Oxygen: Applications in Biosciences and Nanosciences*, Volume 1, S. Nonell, C. Flors. eds., The Royal Society of Chemistry, London, **2016**, 1–21.
[7] R. Gerschman, *Oxygen poisoning and x-irradiation: a mechanism in common*, in: S. Colowick, A. Lazarow, E. Racher, D. R. Schwarz, E. Stadtman, H. Waelsch, eds., Glutathione, Academic Press, Massachusetts, **1954**, 288–291.
[8] J. L. Lugo, E. R. Lugo, M. Puente, *J. Water Health*, **2021**, 19, 20–28.
[9] R. Z. Zhao, S. Jiang, L. Zhang, Z. B. Yu, *Int. J. Mol. Med.*, **2019**, 44, 3–15.
[10] A. Sharma, V. Kumar, B. Shahzad, M. Ramakrishnan, G. P. S. Sidhu, A. S. Bali, N. Handa, D. Kapoor, P. Yadav, K. Khanna, P. Bakshi, A. Rehman, S. K. Kohli, E. A. Khan, R. D. Parihar, H. Yuan, A. K. Thukral, R. Bhardwaj, B. S. Zheng, *J. Plant Growth Regul.*, **2020**, 39, 509–531.
[11] J. Lee, A. R. Han, H. Yu, T. J. Shin, C. Yang, J. H. Oh, *J. Am. Chem. Soc.*, **2013**, 135, 9540–9547.
[12] A. J. Lambert, M. D. Brand, *Methods Mol. Biol.*, **2009**, 554, 165–181.
[13] R. Y. Guo, S. Zong, M. Wu, J. K. Gu, M. J. Yang, *Cell*, **2017**, 170, 1247–1257.
[14] W. Dröge, *Physiol. Rev.*, **2002**, 82, 47–95.
[15] A. Carstensen, A. Herdean, S. B. Schmidt, A. Sharma, C. Spetea, M. Pribil, S. Husted, *Plant Physiol.*, **2018**, 177, 271–284.

Graphical Abstract

Chin. J. Catal., 2022, 43: 1399–1416 doi: 10.1016/S1872-2067(21)63941-4

Electrocatalytic generation of reactive species and implications in microbial inactivation

Forrest Nichols, Kenneth I. Ozoemena, Shaowei Chen *
University of California, United States;
University of the Witwatersrand, South Africa

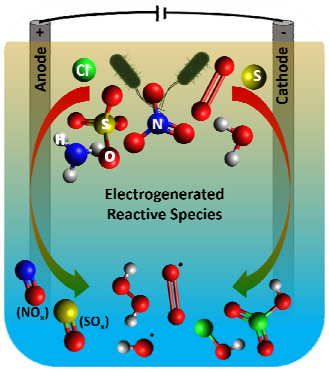

This review summarizes recent progress in the electrochemical production of select reactive species, their interactions with microorganism in water, and practical implementation of such electrochemically generated reactive species for microbial inactivation and water disinfection.

[16] R. Mercado, C. Wahl, J. En Lu, T. Zhang, B. Lu, P. Zhang, J. Q. Lu, A. Allen, J. Z. Zhang, S. Chen, *ChemCatChem*, **2020**, 12, 3230–3239.

[17] B. Lu, Q. Liu, F. Nichols, R. Mercado, D. Morris, N. Li, P. Zhang, P. Gao, Y. Ping, S. W. Chen, *Research*, **2020**, 2020, 9167829.

[18] H. Jiang, J. X. Gu, X. S. Zheng, M. Liu, X. Q. Qiu, L. B. Wang, W. Z. Li, Z. F. Chen, X. B. Ji, J. Li, *Energy Environ. Sci.*, **2019**, 12, 322–333.

[19] J. Z. Li, M. J. Chen, D. A. Cullen, S. Hwang, M. Y. Wang, B. Y. Li, K. X. Liu, S. Karakalos, M. Lucero, H. G. Zhang, C. Lei, H. Xu, G. E. Sterbinsky, Z. X. Feng, D. Su, K. L. More, G. F. Wang, Z. B. Wang, G. Wu, *Nat. Catal.*, **2018**, 1, 935–945.

[20] K. Jiang, J. Zhao, H. Wang, *Adv. Funct. Mater*., **2020**, 30, 2003321.

[21] X. Tian, S. Wang, Z. Wang, H. Wang, Y. Zhou, H. Zhong, Y. Mao, *ChemCatChem*, **2020**, 12, 3240–3248.

[22] D. He, L. Zhong, S. Gan, J. Xie, W. Wang, Z. Liu, W. Guo, X. Yang, L. Niu, *Electrochim. Acta*, **2021**, 371, 137721.

[23] K. Dong, Y. Lei, H. Zhao, J. Liang, P. Ding, Q. Liu, Z. Xu, S. Lu, Q. Li, X. Sun, *J. Mater. Chem. A*, **2020**, 8, 23123–23141.

[24] E. Jung, H. Shin, W. Hooch Antink, Y. Sung, T. Hyeon, *ACS Energy Lett.*, **2020**, 5, 1881–1892.

[25] M. Pelaez, N. T. Nolan, S. C. Pillai, M. K. Seery, P. Falaras, A. G. Kontos, P. S. M. Dunlop, J. W. J. Hamilton, J. A. Byrne, K. O'Shea, M. H. Entezari, D. D. Dionysiou, *Appl. Catal. B*, **2012**, 125, 331–349.

[26] P. P. Fu, Q. S. Xia, H. M. Hwang, P. C. Ray, H. T. Yu, *J. Food Drug Anal.*, **2014**, 22, 64–75.

[27] D. B. Graves, *J. Phys. D Appl. Phys*., **2012**, 45, 263001.

[28] A. Sirelkhatim, S. Mahmud, A. Seeni, N. H. M. Kaus, L. C. Ann, S. K. M. Bakhori, H. Hasan, D. Mohamad, *Nano-Micro Lett.*, **2015**, 7, 219–242.

[29] Q. L. Li, S. Mahendra, D. Y. Lyon, L. Brunet, M. V. Liga, D. Li, P. J. J. Alvarez, *Water Res.*, **2008**, 42, 4591–4602.

[30] C. Barrera-Diaz, P. Canizares, F. J. Fernandez, R. Natividad, M. A. Rodrigo, *J. Mex. Chem. Soc.*, **2014**, 58, 256–275.

[31] N. Gonzalez-Rivas, H. Reyes-Perez, C. E. Barrera-Diaz, *ChemElectroChem*, **2019**, 6, 1978–1983.

[32] I. Linares-Hernandez, C. Barrera-Diaz, B. Bilyeu, P. Juarez-GarciaRojas, E. Campos-Medina, *J. Hazard. Mater.*, **2010**, 175, 688–694.

[33] C. Song, J. Zhang, in: *PEM Fuel Cell Electrocatalysts and Catalyst Layers*, J. Zhang, eds., Springer, New York, **2008**, 89–134.

[34] M. Hayyan, M. A. Hashim, I. M. AlNashef, *Chem. Rev.*, **2016**, 116, 3029–3085.

[35] D. T. Sawyer, J. L. Roberts, *J. Electroanal. Chem*., **1966**, 12, 90–101.

[36] S. Marklund, *J. Biol. Chem.*, **1976**, 251, 7504–7507.

[37] M. Abdollahi, A. Hosseini, in: *Encyclopedia of Toxicology (Third Edition)*, P. Wexler, Eds., Academic Press, Oxford, **2014**, 967–970.

[38] H. Wang, S. Xu, C. Tsai, Y. Li, C. Liu, J. Zhao, Y. Liu, H. Yuan, F. Abild-Pedersen, F. B. Prinz, J. K. Nørskov, Y. Cui, *Science*, **2016**, 354, 1031–1036.

[39] Y. Peng, B. Z. Lu, N. Wang, L. G. Li, S. W. Chen, *Phys. Chem. Chem. Phys*., **2017**, 19, 9336–9348.

[40] Q. Liu, Q. Li, S. Chen, *Curr. Opin. Electrochem*., **2020**, 21, 46–54.

[41] M. Li, Z. Zhao, T. Cheng, A. Fortunelli, C. Chen, R. Yu, Q. Zhang, L. Gu, B. V. Merinov, Z. Lin, E. Zhu, T. Yu, Q. Jia, J. Guo, L. Zhang, W. A. Goddard, Y. Huang, X. Duan, *Science*, **2016**, 354, 1414–1419.

[42] Y. Y. Jiang, P. J. Ni, C. X. Chen, Y. Z. Lu, P. Yang, B. Kong, A. Fisher, X. Wang, *Adv. Energy Mater.*, **2018**, 8, 1801909.

[43] L. Bu, N. Zhang, S. Guo, X. Zhang, J. Li, J. Yao, T. Wu, G. Lu, J. Ma, D. Su, X. Huang, *Science*, **2016**, 354, 1410–1414.

[44] L. Chong, J. G. Wen, J. Kubal, F. G. Sen, J. X. Zou, J. Greeley, M. Chan, H. Barkholtz, W. J. Ding, D. J. Liu, *Science*, **2018**, 362, 1276–1281.

[45] P. Xie, Y. Yao, Z. Huang, Z. Liu, J. Zhang, T. Li, G. Wang, R. Shahbazian-Yassar, L. Hu, C. Wang, *Nat. Commun.*, **2019**, 10, 4011.

[46] X. Tian, X. Zhao, Y. Su, L. Wang, H. Wang, D. Dang, B. Chi, H. Liu, E. J. Hensen, X. W. D. Lou, *Science*, **2019**, 366, 850–856.

[47] L. J. Yang, J. L. Shui, L. Du, Y. Y. Shao, J. Liu, L. M. Dai, Z. Hu, *Adv. Mater*., **2019**, 31, 1804799.

[48] Y. J. Chen, S. F. Ji, S. Zhao, W. X. Chen, J. C. Dong, W. C. Cheong, R. A. Shen, X. D. Wen, L. R. Zheng, A. I. Rykov, S. C. Cai, H. L. Tang, Z. B. Zhuang, C. Chen, Q. Peng, D. S. Wang, Y. D. Li, *Nat. Commun*., **2018**, 9, 5422.

[49] X. L. Tian, X. Zhao, Y. Q. Su, L. J. Wang, H. M. Wang, D. Dang, B. Chi, H. F. Liu, E. J. M. Hensen, X. W. Lou, B. Y. Xia, *Science*, **2019**, 366, 850–856.

[50] E. Brillas, C. A. Martinez-Huitle, *Appl. Catal. B*, **2015**, 166–167, 603–643.

[51] C. A. Martinez-Huitle, E. Brillas, *Appl. Catal. B*, **2009**, 87, 105–145.

[52] I. Sires, E. Brillas, M. A. Oturan, M. A. Rodrigo, M. Panizza, *Environ. Sci. Pollut. Res.*, **2014,** 21, 8336–8367.

[53] S. Garcia-Segura, F. Centellas, C. Arias, J. A. Garrido, R. M. Rodriguez, P. L. Cabot, E. Brillas, *Electrochim. Acta*, **2011**, 58, 303–311.

[54] E. Brillas, R. M. Bastida, E. Llosa, J. Casado, *J. Electrochem. Soc*., **1995**, 142, 1733–1741.

[55] M. H. Zhou, Q. H. Yu, L. C. Lei, G. Barton, *Sep. Purif. Technol*., **2007**, 57, 380–387.

[56] E. Brillas, J. C. Calpe, J. Casado, *Water Res.*, **2000**, 34, 2253–2262.

[57] K. G. Armijos-Alcocer, P. J. Espinoza-Montero, B. A. Frontana-Uribe, C. E. Barrera-Diaz, M. C. Nevarez-Martínez, G. C. Fierro-Naranjo, *Water Air Soil Pollut*., **2017**, 228, 1–8.

[58] H. Barrera, G. Roa-Morales, P. Balderas-Hernandez, C. E. Barrera-Diaz, B. A. Frontana-Uribe, *ChemElectroChem*, **2019,** 6, 2264–2272.

[59] M. Rodriguez-Pena, C. Barrera-Diaz, B. Frontana-Uribe, G. Roa-Morales, *Int. J. Electrochem. Sci.*, **2019**, 14, 4409–4419.

[60] X. G. Duan, H. Q. Sun, S. B. Wang, *Acc. Chem. Res*., **2018**, 51, 678–687.

[61] C. Trellu, E. Mousset, Y. Pechaud, D. Huguenot, E. D. van Hullebusch, G. Esposito, M. A. Oturan, *J. Hazard. Mater*., **2016,** 306, 149–174.

[62] W. Y. Zhu, S. W. Chen, *Electroanalysis*, **2020**, 32, 2591–2602.

[63] C. Tang, Y. Jiao, B. Shi, J. Liu, Z. Xie, X. Chen, Q. Zhang, S. Qiao, *Angew. Chem. Int. Ed*., **2020**, 59, 9171–9176.

[64] E. Jung, H. Shin, B. Lee, V. Efremov, S. Lee, H. S. Lee, J. Kim, W. Hooch Antink, S. Park, K. Lee, S. Cho, J. S. Yoo, Y. Sung, T. Hyeon, *Nat. Mater*., **2020**, 19, 436–442.

[65] X. Shi, S. Siahrostami, G. Li, Y. Zhang, P. Chakthranont, F. Studt, T. F. Jaramillo, X. Zheng, J. K. Nørskov, *Nat. Commun*., **2017**, 8, 701.

[66] V. Viswanathan, H. A. Hansen, J. K. Nørskov, *J. Phys. Chem. Lett*., **2015,** 6, 4224–4228.

[67] S. R. Kelly, X. Shi, S. Back, L. Vallez, S. Y. Park, S. Siahrostami, X. S. Zheng, J. K. Nørskov, *ACS Catal.*, **2019**, 9, 4593–4599.

[68] S. C. Perry, D. Pangotra, L. Vieira, L. Csepei, V. Sieber, L. Wang, C. P. de León, F. C. Walsh, *Nat. Rev. Chem*., **2019,** 3, 442–458.

[69] H. J. H. Fenton, *J. Chem. Soc. Faraday Trans*., **1894**, 65, 899–910.

[70] R. Vasquez-Medrano, D. Prato-Garcia, M. Vedrenne, in: *Advanced Oxidation Processes for Waste Water Treatment*, S. C. Ameta, R. Ameta, Eds., Academic Press, Massachusetts, **2018**, 89–113.

[71] S. O. Ganiyu, M. Zhou, C. A. Martinez-Huitle, *Appl. Catal. B*, **2018**, 235, 103–129.

[72] G. Divyapriya, P. V. Nidheesh, *ACS Omega*, **2020,** 5, 4725–4732.

[73] T. Yu, C. B. Breslin, *Materials*, **2020**, 13, 2254.

[74] H. Sheng, A. N. Janes, R. D. Ross, D. Kaiman, J. Huang, B. Song, J. R. Schmidt, S. Jin, *Energy Environ. Sci*., **2020,** 13, 4189–4203.

[75] G. Li, Y. Zhang, *New J. Chem*., **2019**, 43, 12657–12667.

[76] Q. Wu, J. Wang, Z. Wang, Y. Xu, Z. Xing, X. Zhang, Y. Guan, G. Liao, X. Li, *J. Mater. Chem. A*, **2020,** 8, 13685–13693.
[77] P. Cao, X. Quan, K. Zhao, S. Chen, H. Yu, Y. Su, *Environ. Sci. Technol.*, **2020**, 54, 12662–12672.
[78] R. K. B. Karlsson, A. Cornell, *Chem. Rev.*, **2016**, 116, 2982–3028.
[79] J. Y. Fang, Y. Fu, C. Shang, *Environ. Sci. Technol.*, **2014,** 48, 1859–1868.
[80] R. X. Yuan, S. N. Ramjaun, Z. H. Wang, J. S. Liu, *J. Hazard. Mater.*, **2011**, 196, 173–179.
[81] B. J. Shields, A. G. Doyle, *J. Am. Chem. Soc.*, **2016**, 138, 12719–12722.
[82] Z. H. Wu, J. Y. Fang, Y. Y. Xiang, C. Shang, X. C. Li, F. G. Meng, X. Yang, *Water Res.*, **2016**, 104, 272–282.
[83] J. T. Jasper, Y. Yang, M. R. Hoffmann, *Environ. Sci. Technol.*, **2017**, 51, 7111–7119.
[84] H. Ha, K. Jin, S. Park, K. Lee, K. H. Cho, H. Seo, H. Ahn, Y. H. Lee, K. T. Nam, *J. Phys. Chem. Lett.*, **2019**, 10, 1226–1233.
[85] S. E. Heo, H. W. Lim, D. K. Cho, I. J. Park, H. Kim, C. W. Lee, S. H. Ahn, J. Y. Kim, *J. Catal.*, **2020**, 381, 462–467.
[86] S. Hong, T. K. Lee, M. R. Hoffmann, K. Cho, *J. Catal.*, **2020**, 389, 1–8.
[87] N. Gedam, N. R. Neti, M. Kormunda, J. Subrt, S. Bakardjieva, *Electrochim. Acta*, **2015,** 169, 109–116.
[88] J. Kim, C. Kim, S. Kim, J. Yoon, *J. Ind. Eng. Chem.*, **2018**, 66, 478–483.
[89] T. L. Luu, C. Kim, J. Kim, S. Kim, J. Yoon, *Bull. Korean Chem. Soc.*, **2015**, 36, 1411–1417.
[90] R. E. Palma-Goyes, J. Vazquez-Arenas, C. Ostos, R. A. Torres-Palma, I. Gonzalez, *J. Electrochem. Soc.*, **2016**, 163, H818–H825.
[91] Z. Q. Shi, T. Wang, J. Zhao, R. Qiu, D. X. Duan, C. G. Lin, P. Wang, *Colloids Surf. A*, **2017**, 520, 522–531.
[92] C. Mondelli, A. P. Amrute, F. Krumeich, T. Schmidt, J. Perez-Ramirez, *ChemCatChem*, **2011,** 3, 657–660.
[93] K. Cho, M. R. Hoffmann, *Chem. Mater.*, **2015**, 27, 2224–2233.
[94] C. Comninellis, G. Vercesi, *J. Appl. Electrochem.*, **1991**, 21, 335–345.
[95] N. Menzel, E. Ortel, K. Mette, R. Kraehnert, P. Strasser, *ACS Catal.*, **2013**, 3, 1324–1333.
[96] S. Trasatti, *Electrochim. Acta*, **1987**, 32, 369–382.
[97] R. Ehrenburg, L. Krishtalik, I. Yaroshevskaya, *Elektrokhimiya*, **1975**, 11, 1068–1072.
[98] C. Bruguera-Casamada, I. Sires, E. Brillas, R. M. Araujo, *Sep. Purif. Technol.*, **2017**, 178, 224–231.
[99] P. C. Dedon, S. R. Tannenbaum, *Arch. Biochem. Biophys.*, **2004**, 423, 12–22.
[100] V. I. Bruskov, A. V. Chernikov, V. E. Ivanov, E. E. Karmanova, S. V. Gudkov, *Phys. Wave Phenom*, **2020**, 28, 103–106.
[101] S. Borgmann, *Anal. Bioanal. Chem.*, **2009**, 394, 95–105.
[102] J. P. Werne, D. J. Hollander, T. W. Lyons, J. S. S. Damste, *Geol. Soc. Am. Spec.*, **2004**, 379, 135–150.
[103] E. R. DeLeon, Y. Gao, E. Huang, M. Arif, N. Arora, A. Divietro, S. Patel, K. R. Olson, *Am. J. Physiol. Regul. Integr. Comp. Physiol.*, **2016**, 310, R549–R560.
[104] G. I. Giles, K. M. Tasker, C. Jacob, *Free Radic. Biol. Med.*, **2001,** 31, 1279–1283.
[105] G. I. Giles, M. J. Nasim, W. Ali, C. Jacob, *Antioxidants*, **2017,** 6, 38.
[106] C. Nathan, M. U. Shiloh, *Proc. Natl. Acad. Sci. U. S. A.,* **2000**, 97, 8841–8848.
[107] V. Kapil, R. Khambata, D. Jones, K. Rathod, C. Primus, G. Massimo, J. Fukuto, A. Ahluwalia, *Pharmacol. Rev.*, **2020**, 72, 692–766.
[108] C. Lifshitz, P. J. A. Ruttink, G. Schaftenaar, J. K. Terlouw, H. Schwarz, *Rapid Commun. Mass Spectrom.*, **1987,** 1, 61–63.
[109] N. Zhu, W. P. Shan, Z. H. Lian, Y. Zhang, K. Liu, H. He, *J. Hazard. Mater.*, **2020**, 382, 120970.
[110] K. W. Zha, C. Feng, L. P. Han, H. R. Li, T. T. Yan, S. Kuboon, L. Y. Shi, D. S. Zhang, *Chem. Eng. J.*, **2020**, 381, 122764.
[111] L. P. Han, M. Gao, C. Feng, L. Y. Shi, D. S. Zhang, *Environ. Sci. Technol.*, **2019**, 53, 5946–5956.
[112] P. Bhattacharya, Z. M. Heiden, G. M. Chambers, S. I. Johnson, R. M. Bullock, M. T. Mock, *Angew. Chem. Int. Ed.*, **2019**, 58, 11618–11624.
[113] T. C. Liu, D. Y. Zhang, K. Yin, C. P. Yang, S. L. Luo, J. C. Crittenden, *Chem. Eng. J.*, **2020**, 388, 124264.
[114] H. W. Luo, Y. Cheng, Y. F. Zeng, K. Luo, D. Q. He, X. L. Pan, *Sep. Purif. Technol.*, **2020**, 248, 117023.
[115] M. Alikarami, R. D. C. Soltani, A. Khataee, *Sep. Purif. Technol.*, **2019**, 220, 42–51.
[116] S. D. Jojoa-Sierra, J. Silva-Agredo, E. Herrera-Calderon, R. A. Torres-Palma, *Sci. Total. Environ.*, **2017**, 575, 1228–1238.
[117] S. O. Martikyan, V. A. Shepelin, E. V. Kasatkin, *Sov. Electrochem.*, **1978**, 14, 943–946.
[118] I. Montero-Guadarrama, P. Balderas-Hernandez, C. E. Barrera-Diaz, G. Roa-Morales, *Int. J. Electrochem. Sci.*, **2020**, 15, 7883–7895.
[119] M. Rodriguez-Pena, J. A. B. Perez, J. Llanos, C. Saez, M. A. Rodrigo, C. E. Barrera-Diaz, *Curr. Opin. Electrochem.*, **2021**, 27, 100697.
[120] C. E. Barrera-Diaz, N. Gonzalez-Rivas, in: *Physico-Chemical Wastewater Treatment and Resource Recovery*, R. Farooq, Z. Ahmad, eds., IntechOpen, London, **2017**.
[121] T. Torres-Blancas, G. Roa-Morales, F. Urena-Nunez, C. Barrera-Diaz, A. Dorazco-Gonzalez, R. Natividad, *J. Taiwan Inst. Chem. Eng.*, **2017**, 74, 225–232.
[122] J. A. Lara-Ramos, C. Saez, F. Machuca-Martinez, M. A. Rodrigo, *Sep. Purif. Technol.*, **2020**, 241, 116701.
[123] J. C. Siu, N. Fu, S. Lin, *Acc. Chem. Res.*, **2020**, 53, 547–560.
[124] A. J. Morris, G. J. Meyer, E. Fujita, *Acc. Chem. Res.*, **2009**, 42, 1983–1994.
[125] A. Das, Z. J. Han, W. W. Brennessel, P. L. Holland, R. Eisenberg, *ACS Catal.*, **2015**, 5, 1397–1406.
[126] R. A. Sheldon, I. W. C. E. Arends, *Adv. Synth. Catal.*, **2004**, 346, 1051–1071.
[127] W. J. Shaw, M. L. Helm, D. L. DuBois, *Biochim. Biophys. Acta Bioenergy*, **2013**, 1827, 1123–1139.
[128] C. Lee, D. L. Sedlak, *J. Mol. Catal. A*, **2009**, 311, 1–6.
[129] G. Y. Chen, G. Nunez, *Nat. Rev. Immunol.*, **2010**, 10, 826–837.
[130] K. M. Holmstrom, T. Finkel, *Nat. Rev. Mol. Cell Biology*, **2014**, 15, 411–421.
[131] J. Hou, L. Y. Wang, C. J. Wang, S. L. Zhang, H. Q. Liu, S. G. Li, X. K. Wang, *J. Environ. Sci.*, **2019**, 75, 40–53.
[132] X. W. Liao, S. S. Wang, G. Y. Xu, C. Wang, *ChemElectroChem*, **2019**, 6, 1419–1426.
[133] A. Singh, R. Kukreti, L. Saso, S. Kukreti, *Molecules*, **2019**, 24, 1583.
[134] T. B. Kryston, A. B. Georgiev, P. Pissis, A. G. Georgakilas, *Mutat. Res. Fund. Mol. M.*, **2011**, 711, 193–201.
[135] M. Dizdaroglu, P. Jaruga, *Free Radic. Res.*, **2012**, 46, 382–419.
[136] J. Cadet, T. Douki, J. L. Ravanat, *Free Radic. Biol. Med.*, **2010**, 49, 9–21.
[137] J. Cadet, K. J. A. Davies, *Free Radic. Biol. Med.*, **2017**, 107, 2–12.
[138] D. Prochazkova, I. Bousova, N. Wilhelmova, *Fitoterapia*, **2011**, 82, 513–523.
[139] S. Mateen, S. Moin, A. Q. Khan, A. Zafar, N. Fatima, *PloS One*, **2016**, 11, 0152925.
[140] J. J. Garcia, L. Lopez-Pingarron, P. Almeida-Souza, A. Tres, P. Es-

cudero, F. A. Garcia-Gil, D. X. Tan, R. J. Reiter, J. M. Ramirez, M. Bernal-Perez, *J. Pineal Res.*, **2014**, 56, 225–237.
[141] M. Bains, E. D. Hall, *Biochim. Biophys. Acta. Mol. Basis Dis.*, **2012,** 1822, 675–684.
[142] R. Skouta, S. J. Dixon, J. L. Wang, D. E. Dunn, M. Orman, K. Shimada, P. A. Rosenberg, D. C. Lo, J. M. Weinberg, A. Linkermann, B. R. Stockwell, *J. Am. Chem. Soc.*, **2014**, 136, 4551–4556.
[143] X. L. Shi, N. S. Dalal, K. S. Kasprzak, *Arch. Biochem. Biophys.*, **1993**, 302, 294–299.
[144] A. Torreggiani, M. Tamba, C. Ferreri, *Protein Pept. Lett.*, **2007**, 14, 716–722.
[145] J. Pre, *Sem. Hop.*, **1992**, 68, 1430–1437.
[146] K. H. Cheeseman, *Mol. Asp. Med.*, **1993**, 14, 191–197.
[147] C. Nathan, A. Cunningham-Bussel, *Nat. Rev. Immunol.*, **2013,** 13, 349–361.
[148] C. Staerck, A. Gastebois, P. Vandeputte, A. Calenda, G. Larcher, L. Gillmann, N. Papon, J. Bouchara, M. J. J. Fleury, *Microb. Pathog.*, **2017**, 110, 56–65.
[149] J. Marín-García, *Post-genomic cardiology*, Academic Press, Massachusetts, **2014**.
[150] J. M. McCord, I. Fridovich, *J. Biol. Chem.*, **1969**, 244, 6049–6055.
[151] O. Loew, *Science*, **1900**, 11, 701–702.
[152] G. C. Mills, *J. Biol. Chem.*, **1957**, 229, 189–197.
[153] H. Sies, *Exp. Physiol.*, **1997**, 82, 291–295.
[154] C. Rodriguez, J. C. Mayo, R. M. Sainz, I. Antolin, F. Herrera, V. Martin, R. J. Reiter, *J. Pineal Res.*, **2004**, 36, 1–9.
[155] O. Blokhina, E. Virolainen, K. V. Fagerstedt, *Ann. Bot.*, **2003**, 91, 179–194.
[156] J. A. Imlay, *Annu. Rev. Biochem.*, **2008**, 77, 755–776.
[157] L. J. Marnett, *Carcinogenesis*, **2000**, 21, 361–370.
[158] J. R. Chapman, M. R. G. Taylor, S. J. Boulton, *Mol. Cell,* **2012**, 47, 497–510.
[159] A. Ciccia, S. J. Elledge, *Mol. Cell*, **2010,** 40, 179–204.
[160] L. Masip, K. Veeravalli, G. Georgiou, *Antioxidants Redox Signal.*, **2006**, 8, 753–762.
[161] N. Gong, X. Ma, X. Ye, Q. Zhou, X. Chen, X. Tan, S. Yao, S. Huo, T. Zhang, S. Chen, *Nat. Nanotechnol.*, **2019**, 14, 379–387.
[162] R. G. Chaudhary, A. K. Potbhare, P. Chouke, A. R. Rai, R. K. Mishra, M. F. Desimone, A. A. Abdala, *Mater. Res. Fouda.*, **2020**, 83, 79–116.
[163] M. D. Rojas-Andrade, T. A. Nguyen, W. P. Mistler, J. Armas, J. E. Lu, G. Roseman, W. R. Hollingsworth, F. Nichols, G. Millhauser, A. L. Ayzner, C. Saltikov, S. Chen, *Nanoscale Adv.*, **2020**, 2, 1074–1083.
[164] C. K. Riener, G. Kada, H. J. Gruber, *Anal. Bioanal. Chem.*, **2002**, 373, 266–276.
[165] G. Van Meer, D. R. Voelker, G. W. Feigenson, *Nat. Rev. Mol. Cell Biol.*, **2008**, 9, 112–124.
[166] H. S. El-Beltagi, H. I. Mohamed, *Not. Bot. Horti. Agrobo.*, **2013**, 41, 44–57.
[167] E. Niki, Y. Yoshida, Y. Saito, N. Noguchi, *Biochem. Biophys. Res. Commun.*, **2005**, 338, 668–676.
[168] B. A. Svingen, J. A. Buege, F. O. Oneal, S. D. Aust, *J. Biol. Chem.*, **1979**, 254, 5892–5899.
[169] E. Cabiscol, J. Tamarit, J. Ros, *Int. Microbiol.*, **2000**, 3, 3–8.
[170] T. Grune, K. Merker, G. Sandig, K. J. Davies, *Biochem. Biophys. Res. Commun.*, **2003**, 305, 709–718.
[171] J. T. Tansey, *Biochemistry: An integrative approach*, John Wiley & Sons, New Jersey, **2020**, 1.
[172] T. Yamaza, K. F. Masuda, I. Atsuta, K. Nishijima, M. A. Kido, T. Tanaka, *J. Dent. Res.*, **2004**, 83, 619–624.
[173] C. L. Limoli, M. I. Kaplan, E. Giedzinski, W. F. Morgan, *Free Radical. Bio. Med.*, **2001**, 31, 10–19.
[174] J. Cadet, J. R. Wagner, *Cold Spring Harb. Perspect. Biol.*, **2013**, 5, a012559.
[175] C. Badouard, M. Masuda, H. Nishino, J. Cadet, A. Favier, J. L. Ravanat, *J. Chromatogr. B*, **2005**, 827, 26–31.
[176] S. Cotillas, J. Llanos, M. A. Rodrigo, P. Canizares, *Appl. Catal. B*, **2015**, 162, 252–259.
[177] D. Ghernaout, M. Aichouni, M. Touahmia, *Desalin. Water Treat.*, **2019**, 141, 68–81.
[178] D. Ghernaout, A. Badis, A. Kellil, B. Ghernaout, *Desalination*, **2008**, 219, 118–125.
[179] D. Ghernaout, B. Ghernaout, *Desalin. Water Treat.*, **2010**, 16, 156–175.
[180] J. N. Hakizimana, N. Najid, B. Gourich, C. Vial, Y. Stiriba, J. Naja, *Chem. Eng. Sci.*, **2017**, 170, 530–541.
[181] E. J. La Motta, G. J. Rincon, L. E. De Grau, K. D. Jovanovich, *J. Environ. Eng.*, **2018**, 144, 04017090.
[182] J. Llanos, S. Cotillas, P. Canizares, M. A. Rodrigo, *Ultrason. Sonochem.*, **2015**, 22, 493–498.
[183] J. Llanos, S. Cotillas, P. Canizares, M. A. Rodrigo, *Water Res.*, **2014**, 53, 329–338.
[184] W. T. Mook, M. K. Aroua, G. Issabayeva, *Renew. Sustain. Energy Rev.*, **2014**, 38, 36–46.
[185] A. R. Rahmani, D. Nematollahi, A. Poormohammadi, G. Azarian, F. Zamani, *Chemosphere*, **2021**, 263, 127761.
[186] L. A. M. L. Sanchez, M. A. L. Lit, *Philipp. J. Crop Sci.*, **2018**, 43, 20–26.
[187] A. Simas, R. Mores, J. Steffens, R. M. Dallago, A. Kunz, W. Michelon, G. Fongaro, A. Viancelli, *Environ. Chem. Lett.*, **2019**, 17, 495–499.
[188] L. Chen, Y. L. Xu, X. F. Dong, C. F. Shen, *Environ. Eng. Sci.*, **2020**, 37, 783–789.
[189] S. Cotillas, P. Canizares, M. J. M. de Vidales, C. Saez, M. A. Rodrigo, J. Llanos, *Chem. Eng. Trans.*, **2014**, 133–138.
[190] S. Cotillas, J. Llanos, O. G. Miranda, G. C. Diaz-Trujillo, P. Canizares, M. A. Rodrigo, *Electrochim. Acta*, **2014**, 140, 396–403.
[191] J. Ding, K. Wang, S. N. Wang, Q. L. Zhao, L. L. Wei, H. B. Huang, Y. X. Yuan, D. D. Dionysiou, *Chem. Eng. J.*, **2018**, 344, 34–41.
[192] J. Ding, Q. L. Zhao, J. Q. Jiang, L. L. Wei, K. Wang, Y. S. Zhang, W. Z. Hou, H. Yu, *Environ. Sci. Pollut. Res.*, **2017**, 24, 5152–5158.
[193] D. Ghernaout, M. W. Naceur, A. Aouabed, *Desalination*, **2011**, 270, 9–22.
[194] J. Isidro, D. Brackemeyer, C. Saez, J. Llanos, J. Lobato, P. Canizares, T. Matthee, M. A. Rodrigo, *Sep. Purif. Technol.*, **2019**, 208, 110–115.
[195] S. Cotillas, J. Llanos, I. Moraleda, P. Canizares, M. A. Rodrigo, *Chem. Eng. J.*, **2020**, 380, 122415.
[196] X. Qi, T. Wang, Y. Long, J. Ni, *Sci. Rep.*, **2015**, 5, 10388.
[197] X. Huang, Y. Qu, C. A. Cid, C. Finke, M. R. Hoffmann, K. Lim, S. C. Jiang, *Water Res.*, **2016**, 92, 164–172.
[198] A. Ahmadi, T. Wu, *Environ. Sci. Water Res. Technol.*, **2017**, 3, 534–545.
[199] E. Brillas, B. Boye, I. Sires, J. A. Garrido, R. M. Rodriguez, C. Arias, P. L. Cabot, C. Comninellis, *Electrochim. Acta*, **2004**, 49, 4487–4496.
[200] P. Canizares, C. Saez, J. Lobato, M. A. Rodrigo, *Ind. Eng. Chem. Res.*, **2004**, 43, 1944–1951.
[201] E. A. Ekimov, V. A. Sidorov, E. D. Bauer, N. N. Melnik, N. J. Curro, J. D. Thompson, S. M. Stishov, *Nature*, **2004**, 428, 542–545.
[202] H. B. Suffredini, V. A. Pedrosa, L. Codognoto, S. A. S. Machado, R. C. Rocha, L. A. Avaca, *Electrochim. Acta*, **2004**, 49, 4021–4026.
[203] S. Cotillas, J. Llanos, P. Canizares, S. Mateo, M. A. Rodrigo, *Water*

Res., **2013**, 47, 1741–1750.
[204] J. V. Macpherson, *Phys. Chem. Chem. Phys.*, **2015**, 17, 2935–2949.
[205] J. O. Thostenson, E. Ngaboyamahina, K. L. Sellgren, B. T. Hawkins, J. R. Piascik, E. J. D. Klem, C. B. Parker, M. A. Deshusses, B. R. Stoner, J. T. Glass, *ACS Appl. Mater. Interfaces*, **2017**, 9, 16610–16619.
[206] Y. Sato, M. Kamo, in: *the Properties of Natural and Synthetic Diamond*, J. E. Field, eds., Academic Press, London, **1992**, 423–469.
[207] D. M. de Araujo, P. Canizares, C. A. Martinez-Huitle, M. A. Rodrigo, *Electrochem. commun*., **2014**, 47, 37–40.
[208] O. A. Williams, *Diam. Relat. Mater.*, **2011**, 20, 621–640.
[209] J. Wang, M. A. Firestone, O. Auciello, J. A. Carlisle, *Langmuir*, **2004**, 20, 11450–11456.
[210] J. O. Thostenson, R. Mourouvin, B. T. Hawkins, E. Ngaboyamahina, K. L. Sellgren, C. B. Parker, M. A. Deshusses, B. R. Stoner, J. T. Glass, *Water Res*., **2018**, 140, 191–199.
[211] K. Jiang, S. Back, A. J. Akey, C. Xia, Y. Hu, W. Liang, D. Schaak, E. Stavitski, J. K. Nørskov, S. Siahrostami, *Nat. Commun.*, **2019**, 10, 3997.
[212] Y. X. Wang, H. Y. Su, Y. H. He, L. G. Li, S. Q. Zhu, H. Shen, P. F. Xie, X. B. Fu, G. Y. Zhou, C. Feng, D. K. Zhao, F. Xiao, X. J. Zhu, Y. C. Zeng, M. H. Shao, S. W. Chen, G. Wu, J. Zeng, C. Wang, *Chem. Rev.*, **2020**, 120, 12217–12314.
[213] Y. Peng, B. Z. Lu, S. W. Chen, *Adv. Mater.*, **2018**, 30, 1801995.
[214] S. Toze, *Water Res*., **1999**, 33, 3545–3556.
[215] M. Steele, J. Odumeru, *J. Food Prot.*, **2004**, 67, 2839–2849.
[216] P. T. J. Johnson, S. H. Paull, *Freshw. Biol.*, **2011**, 56, 638–657.
[217] C. Guzman, J. Jofre, M. Montemayor, F. Lucena, *J. Appl. Microbiol.*, **2007**, 103, 2420–2429.
[218] R. Armon, D. Gold, M. Brodsky, G. Oron, *Water Sci. Technol.*, **2002**, 46, 115–122.
[219] N. Abreu-Acosta, L. Vera, *Ecol. Eng.*, **2011**, 37, 496–503.
[220] T. T. Fong, E. K. Lipp, *Microbiol. Mol. Biol. Rev*., **2005**, 69, 357–371.
[221] W. A. M. Hijnen, E. F. Beerendonk, G. J. Medema, *Water Res*., **2006**, 40, 3–22.
[222] M. D. Rojas-Andrade, G. Chata, D. Rouholiman, J. L. Liu, C. Saltikov, S. W. Chen, *Nanoscale*, **2017**, 9, 994–1006.
[223] M. Planchon, T. Leger, O. Spalla, G. Huber, R. Ferrari, *PloS One*, **2017**, 12, e0178437.
[224] Q. Ma, J. Zhou, W. W. Zhang, X. X. Meng, J. W. Sun, Y. J. Yuan, *PloS One*, **2011**, 6, e26108.
[225] D. D. Chang, Z. S. Yu, Z. Ul Islam, W. T. French, Y. M. Zhang, H. X. Zhang, *Biotechnol. Biofuels*, **2018**, 11, 283.

反应性物种的电催化生成及其对微生物灭活的影响

Forrest Nichols [a], Kenneth I. Ozoemena [b], 陈少伟[a,*]
[a]加利福尼亚大学化学与生物化学系, 加利福尼亚, 美国
[b]金山大学化学学院, 分子科学研究所, 约翰里司堡, 南非

摘要: 控制水系统(包括废水、娱乐用水和饮用水)中的微生物增殖对社会健康至关重要. 电催化反应产生的反应性物质(RS)可以作为介导来使微生物失活, 从而为控制微生物生长提供了有效途径. 本文概述了电催化反应产生RS及其应用于水消毒的最新进展, 重点介绍了RS的选择性生产、微生物与RS的相互作用(包括RS作用机制和微生物对RS的先天反应), 以及催化反应产生的RS用于微生物灭活的实际应用. 本文还展望了基于RS的水电化学消毒的挑战和机遇以及未来可能的研究方向.

关键词: 电催化; 活性物种; 微生物; 灭活; 水电化学消毒

收稿日期: 2021-07-15. 接受日期: 2021-09-08. 上网时间: 2022-04-20.
*通讯联系人. 电子信箱: shaowei@ucsc.edu
基金来源: 国家科学基金(CBET-1848841, CHE-1900235).
本文的电子版全文由Elsevier出版社在ScienceDirect上出版(http://www.sciencedirect.com/journal/chinese-journal-of-catalysis).